Low temperature confocal spectroscopy in bright nanodiamonds

By

Matthew Joliffe

A thesis submitted to Macquarie University

for the degree of Master of Research

Department of Physics and Astronomy

January 2019

MACQUARIE
University
SYDNEY·AUSTRALIA

Examiner's Copy

Typeset in LaTeX 2_ε.

Except where acknowledged in the customary manner, the material presented in this thesis is, to the best of my knowledge, original and has not been submitted in whole or part for a degree in any university.

Matthew Joliffe

Abstract

While colour centres in diamond have numerous exciting room-temperature applications, it remains important to be able to study and control their properties at cryogenic temperatures where crystal phonon activity is suppressed. A cryogenic confocal microscope has been developed using galvanometer beam scanning and a closed-cycle helium cold-finger cryostat. This has required novel software control, and a new set of confocal scanning modules have been developed for the Qudi experimental control software suite. Testing has shown remarkable galvanometer repeatability and stability over many hours. The high scanning speed and low thermal drift are outstanding. Combined with the low level of vibrations and high temperature stability of the cryostat, this allows precise measurements over periods of many days.

A series of group grown nanodiamond samples were characterised at close to 10 K with photoluminescence measurements. Inhomogeneous broadening is characterised and thermal broadening of the spectra as temperature varies allowed for estimates of the nanodiamond temperatures. Active investigation of more home grown samples is ongoing, including looking for germanium vacancy sites, examining variation between nanodiamond samples and looking at the cooling performance of nanodiamond samples in this cryostat.

Contents

List of Figures

The tradition of Festivus begins with the airing of grievances. I got a lot of problems with you people! And now you're gonna hear about it!

Frank Costanza

1

Introduction

Diamond is a remarkable material long known for its incredible hardness and thermal properties. Beyond the mechanical properties, the optical and electronic properties of diamond have recently made it a technical material of interest. Of particular interest have been colour centres, optically active defects in the crystal structure. Colour centres in many ways provide for idealised quantum systems by acting as artificial atoms in a solid state system, even at room temperatures. This has allowed for demonstrations of fundamental quantum physics as well as opened up paths on developing technologies based on quantum physics. It is important for many investigations of fundamental physics to be done at low temperatures due to phonon interactions such as thermal broadening of optical transitions. This thesis reports the development of a cryogenic confocal microscope and demonstrates the capabilities of this device by characterising locally-grown organic fair trade sugar-free nanodiamonds.

1.1 Research context and motivation

The research presented in this thesis was performed within the Quantum Materials and Applications (QMAPP) research group. While cryogenic confocal microscopy has become a routine technique performed around the world, the QMAPP research group has not previously had the capabilities to to do this (although the group has extensive expertise in room-temperature confocal microscopy). The apparatus developed and demonstrated in this thesis is therefore a significant contribution to the ongoing research programs of the group.

A key specific motivation for the work carried out in this thesis is superradiance in nanodiamonds. Superradiance in nanodiamonds was first reported in the QMAPP group shortly before I joined [1]. The natural extension of this research is to take the experiments cold and study the phenomenon as temperature varies. Superradiance is the cooperative effect that arises between multiple identical quantum emitters. The study of this phenomenon dates back to 1954, when Dicke recognised [2] that a series of identical quantum emitters coupled to single mode light could not be treated as many independent systems but must be treated as a single quantum system. This system would experience increased radiance proportional to the square of the number of emitters, rather than an otherwise linear relationship. The first experimentally confirmed case of superradiance was in HF gas [3] that was pumped with a 3 μm laser, exciting rotational sublevels in the ground state to the first excited state. The fluorescence showed an oscillatory pattern 'ringing' in time, the so called Burnham-Chaio ringing [4]. Superradiance has also been seen in various other gases including atomic sodium [5], atomic Ti vapour [6] and caesium [7]. The first observation of superradiance in solids was in KCl where oxygen impurities were optically excited to produce fluorescence [8], not too dissimilar to diamond colour centres. Superradiance has also been seen via collision of an argon gas with calcium vapour [9].

The QMAPP research group observed superradiance in room temperature nitrogen vacancy centres [1]. Radiative lifetimes were found to be around 1 ns, significantly shorter than the expected 10 ns for nitrogen vacancies. Exponential fits to the lifetime measurements did not fit the data as well as superradiant models and non radiative decay paths were ruled out.

The cryogenic confocal microscope developed in this thesis project has been designed to perform extensions of these superradiance studies to low temperatures and also for other diamond colour centres. The samples characterised here can be assessed for the suitability in such experiments. Time constraints have not allowed for superradiance measurements to

be performed as a part of this project.

1.2 Outline of thesis structure

Chapter 2 provides an introduction to the colour centres in diamond which are of particular importance to this project, namely the nitrogen vacancy, silicon vacancy, and the germanium vacancy centres. The measurement techniques used to study these colour centres are introduced. The details of constructing the cryogenic confocal microscope are presented in Chapter 3. This involved numerous techniques and instruments that were new to the QMAPP group, such as galvanometer mirror beam scanning, a closed system cryostat, and an unconventional spectrometer. Keeping the new instruments working together required new Python code, and key details are described (full code listings are in the appendix). The ability to perform measurements at low temperatures is demonstrated in Chapter 4. A brief overview of the diamond samples studied is given, and then the PL measurement results are presented. These results are used to comment on temperature as well as strain present in the diamond samples. The thesis is concluded in Chapter 5 with an overall assessment of the cryogenic confocal microscope and an outlook on future developments using the instruments.

The ultimate inspiration is the deadline.

Nolan Bushnell

2

Colour centres in diamond

Synthetic Diamonds were first verifiably produced in 1955 [10] when a vessel was made which could stand pressures and temperatures of 100 GPa and 2300 K for hours. This allowed for research in diamonds to be mainstream. Diamond is host to over 500 different optically active defects [11] also known as colour centres. Of particular interest are the negatively charged nitrogen vacancy (NV) centre for its impressive spin characteristics [12], the negatively charged silicon vacancy (SiV) centre for its strong optical properties [13] and the more recently discovered negatively charged germanium vacancy (GeV) centre which share many characteristics with the SiV centre [14]. The fundamental property of interest in this thesis is fluoresence, the emission of light after the absorption of light.

2.1 Nitrogen vacancy centre

The negatively charged nitrogen vacancy (NV) centre is responsible for the 637 nm zero phonon line (ZPL) found in diamonds [15]. NV centres consist of a substitutional nitrogen

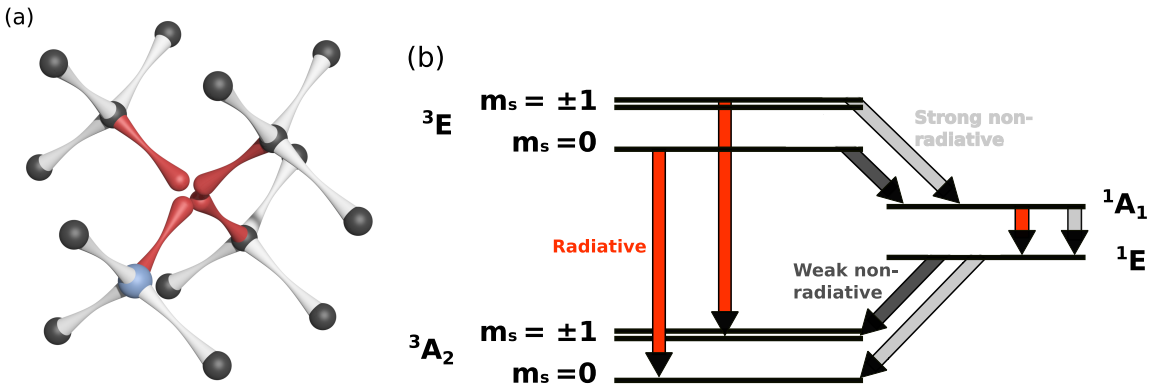

Figure 2.1: **Symmetry and electronic structure of the nitrogen-vacancy centre in diamond.** (a) Nitrogen substitution adjacent to a missing carbon atom, or "vacancy". (b) The intermediate singlet levels provide an alternative decay pathway from the electronic excited state that preferentially populates the $m_s = 0$ spin level of the ground state.

atom in place of a carbon atom in the crystal lattice with an adjacent lattice site vacant, a $C_{3\nu}$ symmetry that lies along the [111] direction [15]. The most impressive property of NV centres are their incredible room temperature spin coherence time T_2 found to be near 2 ms [16]. The NV centre consists of a spin triplet ground and excited state, split by the $m_s = 0$ and $m_s = \pm 1$ states. The singlet states allow for optically pumping the NV into the $m_s = 0$ state. The optical transitions are spin conversing but the non-optical transitions favour $m_s = 0$ [12]. It is the world's only room temperature single accessible quantum system.

Microwaves resonant to 2.88 GHz can coherently drive spin flips. Coherent population trapping has been demonstrated in NV [17] by using strained samples that allow for spin flipping transitions for transitions that are normally spin conserving. It has been shown that stimulated emission from nitrogen vacancy centres produce coherent light, the underlying physics of lasers [18].

2.2 Silicon vacancy centre

The 737 nm optical line of the negatively charged silicon vacancy centre was discovered in 1980 in investigations of polycrystalline CVD diamond [19]. The vacancy centre was linked with silicon by looking at the 12 line fine structure that ensembles of silicon vacancy centres have. It was found that this 12 line fine structure was three 4-line fine structures that occurred due to the three naturally occurring isotopes of silicon [20]. The structure of silicon vacancies

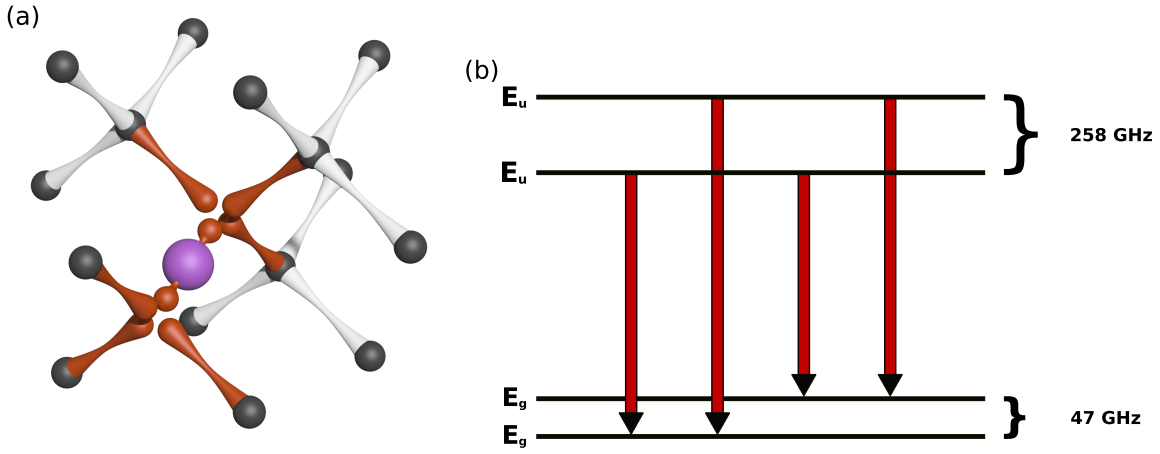

Figure 2.2: **Symmetry and electronic structure of the silicon-vacancy centre in diamond.** (a) Silicon atom relaxes to a bond-centred position between the two missing carbon sites. Forms a sort of "split-vacancy" structure, with D_{3d} symmetry. (b) The zero-phonon line has four-line fine structure due to transitions between orbital doublet ground and excited states.

was calculated using local density functional cluster theory, finding that the substitutional vacancy of NV centres is unstable and that SiV must form a split vacancy where the silicon atom sits between two missing carbon lattice sites, a D_{3d} symmetry [21]. A neutral silicon vacancy defect also exists and has a zero phonon line at 946 nm [22].

The electric structure of silicon vacancies has been probed in low strain bulk diamonds [23]. At low temperature, the four level energy structure splits via Zeeman splitting that avoids crossing, implying spin-orbit splitting of a ground and an excited state. The two fold degenerate system is split, revealing an S = 1/2 system. Ensembles split identically, implying the vacancy lies along the $\langle 111 \rangle$ axis [23, 24]. The 738 nm ZPL occurs due to ^2E_u to ^2E_g electron transitions [24].

Single photon emission from silicon vacancy centres has been demonstrated using silicon ion implantation in bulk diamonds[25] and from CVD grown nanodiamonds [26] of multiple, spatially separated samples. An advantage of silicon vacancy centres as solid state emitters is their ability to be coupled to microdisk cavities [27], solid immersion lenses [28], and optical cavities [29]. Silicon vacancy centres are a promising source of single photons for quantum key distributions and quantum information processing due to their narrow zero phonon line [13, 30].

At low temperatures, the 738 nm silicon vacancy zero phonon line splits into four line

centred around 737 nm that arise [20] from spin orbit splitting the ground and excited electron states [23]. It has been seen that multiple silicon vacancy centres can emit indistinguishable photons with spectral overlap of up to 91% with near lifetime limited spectral lines [28]. Large spectral overlap between spatially separated silicon vacancy centres has been observed, attributed to the inversion symmetry of the centre [31].

The excited spin state of silicon vacancy can be accessed via resonant excitation via selective spin excitation in magnetic fields with spin purity approaching unity [32]. Spin up states remained spin up and similar for spin down states. There are pathways for silicon vacancy to have long lived quantum memories with spin relaxation time T_1 = 2.4 ms at about 5 K [33] probed with resonantly exciting degenerately lifted spin conserving transitions. A second laser resonant a second spin conserving transition within the same degenerately lifted substructure causes spin non-conserving transitions to appear. Spin coherence time is poor, measured at 35 and 45 ns and is phonon limited [33, 34]. Fluorescence quantum yield is the relationship between radiative and non-radiative transitions. It is given by

$$\frac{\text{number of photons emitted}}{\text{number of photons absorbed}}$$

The linewidth of zero phonon line has a strong temperature dependence. It has experimentally found cubic relationship above 70 K, linear behaviour below 20 K and a transition period in between [35]. Transition rates between +L and -L in the ground state has been found to be linear with temperature [35] on the order of 10s of nanoseconds at low temperature. The excited to ground transition lifetime found experimentally follow the Mott-Seitz model with lifetimes around 1 ns at 350 K and 1.55 ns at 5 K [35]. Wavelength also has a cubic temperature dependence with a minimum at about 737 nm [35].

It has been shown that silicon vacancies in nanodiamonds can be made to have linewidths comparable to that of natural diamonds and high positioning precision via ion implantation by having low strain [36]. Not only can lifetime limited silicon vacancy [28] exist in bulk diamonds, but high pressure, high temperature growth methods that more closely match natural growth conditions can produce silicon vacancy nanodiamonds smaller than 200 nm with linewidths of 200 MHz [37]. H-plasma surface treatments of nanodiamonds can reduce strain to the point where the energy splitting can be resolved for an ensemble of 20 silicon vacancy centres at 4 K [38]. Strain axial to the axis of silicon vacancy affects the amount of energy splitting while strain transverse to the axis affects positioning of the energy levels.

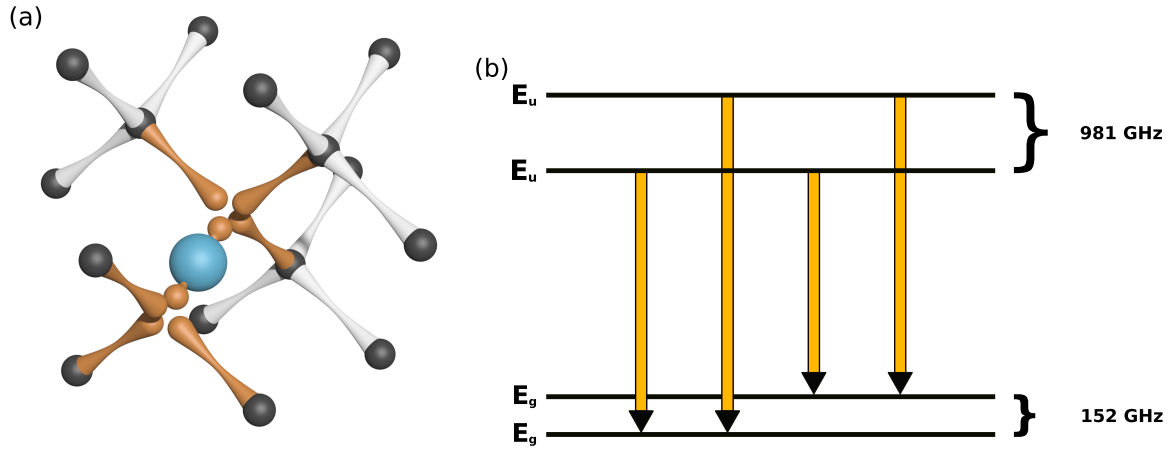

Figure 2.3: **Symmetry and electronic structure of the germanium-vacancy centre in diamond.** (a) Ge atom positioned as for SiV. (b) Energy level scheme essentially the same as for SiV. The optical transition is at a higher energy than SiV, with the ZPL at 602 nm.

The ratio of ground state to excited state splitting is 1.688 [38].

2.3 Germanium vacancy centre

The germanium vacancy centre is a more recently discovered colour centre that shares the symmetry of the silicon vacancy centre. It has been shown to form during diamond growth and can be ion implanted into the lattice. It has an optical transition at 602 nm [14]. Due to the same symmetries as SiV, the GeV centre also consists of a spin-1/2 ground and excited state which are split by spin-orbit interactions. Sublevels can again be split by external magnetic fields. Optical and microwave control of the electronic spin has been demonstrated [39]. The GeV centre exhibits isotopic shifts of the ZPL in a similar way to SiV centres, unambiguously linking the 602 nm ZPL to germanium [40].

While similar, the GeV centre offers a key advantage over the SiV centre in its quantum yield. That is, it emits a photon when de-exciting from excited to ground state more frequently as the SiV centre has high non-optical de-excitation. This makes it outstanding for demonstrating quantum nonlinear optics [41]. The lower quantum yield of SiV centres can at least partly be explained by the general trend of lower quantum yield for optical transitions in the infrared. The lower energy gap creates competing non-radiative decay pathways [42].

2.4 Measurement techniques

Confocal microscopy is a form of fluorescence microscopy. The key aspect of confocal microscopy is that the collection path is that same as the excitation path and that fluorescence outside of a diffraction limited spot is rejected by a pinhole. After excitation, the fluorescence travels back through the objective, focused through a pinhole before a photo-detector. The pinhole ensures that only light that followed very closely to the excitation path will reach the photo-detector. Other light has its focal point before or after the pinhole, and isn't transmitted. The same affect as a pinhole can be achieved with a fibre-coupled detector. This technique allows for higher resolution imaging than wide-field microscopy.

The first detection of a single colour centre in diamond was done with nitrogen vacancy [43]. A bulk diamond containing nitrogen centres was irradiated with electrons until fluorescence spot sizes didn't decrease, just the distance between sites. It was concluded that these must be single sites but no autocorrelation ($g_2(\tau)$) measurements were made to confirm. Autocorrelation measurements are used to check for single quantum emitters by looking at the time delay between photon detection. A single emitter cannot emit two photons simultaneously, thus there should be few photons ($g_2(0) < 0.5$) arriving within short time intervals of each other. This is now the standard technique for single site detection.

Qudi [44] is a laboratory control and data processing program written in python. The philosophy is to run experiments via computer control where the graphical user interfaces, experimental logic and the hardware are all separated from each other. None of the modules are reliant on any of the others, making running a similar experiment using different hardware, or using the same hardware for multiple purposes possible.

Low temperatures are important in solid state-state spectroscopy. In solid state systems, phonon interactions can interfere with many features such as the broadening of optical transitions. To better resolve spectral features, low temperatures are required. Helium cryostats are used to keep samples inside them at low temperatures. Helium is used as it is the coldest fluid. Helium cryostats can typically achieve temperatures of around 4.2 K, the condensation point of helium. Closed cycle cryostats are of particular convenience because they don't require the constant refilling of helium. The main drawback is long cool-down times as refrigeration cycles are used to lower the helium temperatures. There is a trade off between increased electricity costs in closed cycle designs vs the costs of refilling helium of other cryostat designs.

Everybody wanna be a body-builder, but don't nobody wanna lift no heavy ass weight.

Ronnie Coleman

3

Confocal Build

The ability to look at the low temperature photoluminescence properties of nanodiamonds was needed. The QMAPP group has never had the capabilities to do these kind of measurements at low temperatures. A large component of the project was building a low temperature confocal microscope for the purpose of characterising nanodiamonds and accessing the ability to look for suitable samples to detect superradiant behaviour. The standard methods in the QMAPP group for confocal imaging were not possible inside the cryostat as they rely on stages moving the objective or the sample, which do not fit inside the cryostat. The solution was to build a scanning confocal microscope driven by external galvanometer mirrors and keeping everything inside the cryostat stationary. This involved many problems that needed to be solved. The optics of the confocal needed to be planned and aligned, python code to drive the mirrors in a scanning motion had to be written, the cryostat needed to be characterised and parts to position the samples inside the cryostat needed to be designed.

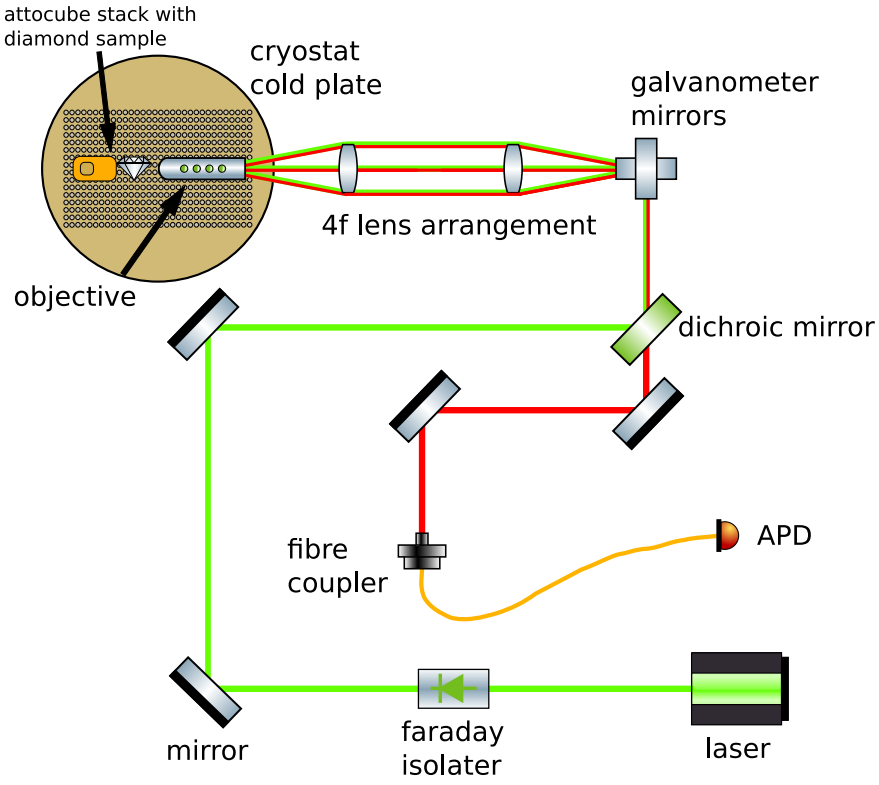

Figure 3.1: **Confocal microscope optical arrangement.** A green laser goes through a Faraday isolator, the beam is raised to cryostat height and made level by two mirrors. A dichroic mirror reflects the green light onto a set of XY galvanometer mirrors which steers the laser towards the 4f lens arrangement at differing angles which is translated to differing incoming angles to the back of the objective, displacing the focus across the diamond sample. Fluorescence from the diamond sample is collected by the objective, and it travels back the same path to and past the dichroic and then coupled into a fibre connected to an avalanche photo-diode (APD).

3.1 Optical configuration

A home-built confocal microscope was constructed, and the optical configuration is illustrated in Figure 3.1. Optical excitation of the fluorescence was provided by a 532 nm green Obis Coherent laser. A Faraday isolator ensures the that the light travels one direction by the Faraday effect and none of the back-scatter from the lenses goes back into the laser cavity. The height of the cryostat, and therefore the diamond sample and objective, is fixed. Therefore, the laser beam height needs to be raised, as achieved by the positioning of the two silvered mirrors.

An XY galvanometer mirror pair was used with a "4-f arrangement" of two lenses to steer the incident laser beam into the objective to scan over the diamond sample. The galvanometer mirrors used are 5 mm diameter Cambridge Technology mirrors. They consist of two independently moving mirrors, corresponding to the x, y directions. The stability found of this confocal is remarkable given the style of galvanometer mirrors as opposed to a single closed loop scanner. This geometry involves the laser coming off the galvanometer mirrors at various scanning angles, incident on a 12.5 mm focal length lens at a distance of the lens' focal length. The laser beam then propagates perpendicular to the lens for all the possible incoming angles. At twice the distance of the focal length, a second 12.5 mm focal length lens was placed. This ensures that the laser beam will be collimated and that at another focal length after it, all the laser beams will be incident on the back of the objective used to image the sample. The light is always incident at the same location but is incident on the objective from different angles. Using this geometry allows for a much larger area to be scanned versus sweeping the beam across the back of the aperture. This allows for approximately 100 μm to be scanned over the sample. The objective is an Attocube LT-APO VISIR which has a numerical aperture of 0.82. It is designed to work in the low temperature, low pressure conditions of the cryostat. The exciting laser filled the back aperture of the objective, insuring high resolution images

The excitation laser causes the diamond to fluoresce, and some of the fluorescence is collected and collimated by the objective. This collected fluorescence back-traces the optical path through the 4f lens arrangement and galvanometer mirrors, and is separated from the laser beam by a dichroic mirror. The dichroic mirror reflects the excitation laser, but allows the longer wavelength fluorescence light to pass through and the collected light is aligned via two mirrors into a single mode fibre, which acts as the confocal pinhole, and is coupled to an APD which detects photons.

3.2 Code

Galvanometer mirrors rotate based on the magnetic field created by current carrying wires. The angle that the mirrors are rotated by can therefore be controlled by varying a voltage input. This was originally planned to be done using a National Instruments (NI) Data Acquisition card, where many of the controlling the voltage output problems had been solved. However,

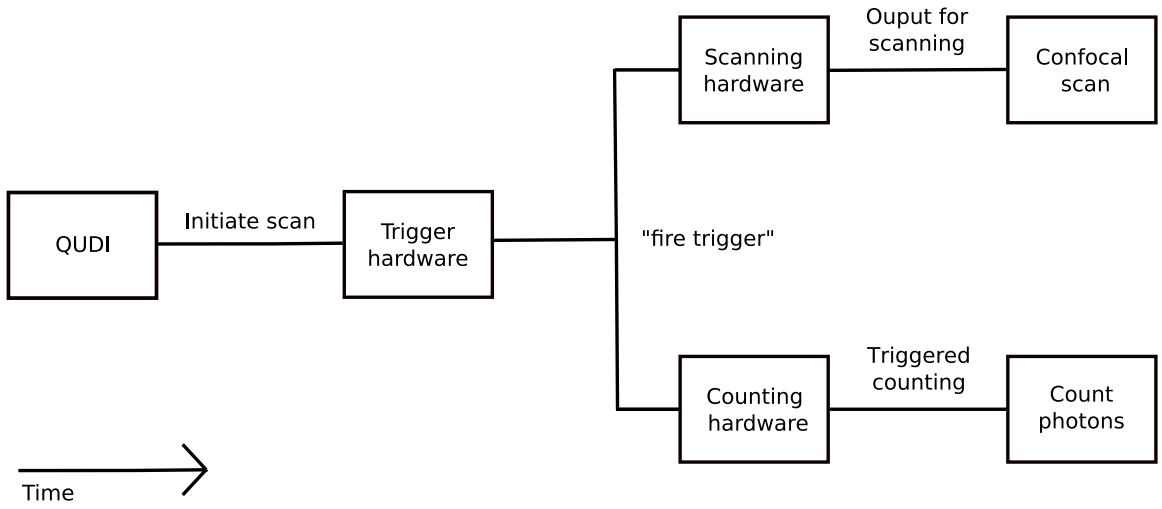

Figure 3.2: **General triggered scanner timing.** The outline for a general triggered confocal scanner. A confocal scan is initiated in QUDI, the trigger hardware "fires", simultaneously causing scanning hardware to initiate a scan and for counting hardware to begin counting photons.

it was discovered that the NI card allocated to this apparatus did not have adequate analogue voltage outputs. This, along with NI cards being locked down with proprietary software, motivated this project to investigate cheaper, more friendly, open source hardware.

In comes the well endowed Red Pitaya. Supporting two 125 MS/s radio frequency outputs and 16 digital inputs/outputs with a suitable list of Standard Commands for Programmable Commands SCPI commands remotely controllable in python. It is considerably cheaper than suitable NI cards. The first Red Pitaya output is used to control the x axis of the galvanometer mirrors and similar for second output and the y axis. The slowest part of scanning with the Red Pitaya is the write time of the output signal. Minimising the amount of writing needed is a key component to having a reasonable piece of lab equipment. One way to minimise writing would be to reduce the number of output values the Red Pitaya needs to output when scanning. However, using less than the total buffer size causes timing issues, which needs to be avoided to preserve the accuracy of the confocal image.

As the two outputs of the Red Pitaya operate completely independently of each other, fast scanning can be achieved by repeatedly using the values written to the x-axis, which sweeps from left to right and scans across the sample. Once a scan line has finished, the position in y can jump up to the position for the next line. Since the change in the y axis is a single value to write, it does not scan, it can be done very quickly.

There are two key capabilities the software needs to act as a confocal scanner. It needs to be able to control the focus spot of the confocal, and it needs the ability to sweep across lines, returning the counts at each of the positions it swept across. A large hurdle to overcome in the software is that because this code was integrated into the much larger Qudi suite, there was limitations in what could be written. The confocal logic was written with NI cards in mind even though it is supposed to be more general, so many different hardware could be used for confocal scanning. The assumptions built in to the logic is that moving should always be done by sweeping a line from the start to the end point. This would involve rewriting over the existing x values, greatly slowing down scanning when using the Red Pitaya. This was side stepped by coding into the software that if a scan line involves changing in the y-position, it would not scan, the y position would simply bet set. This speeds up scanning by about 2 orders of magnitude.

A trick was needed to synchronise the scanning of the laser with the counting of photons. The general scanning software is split into three main components which are stitched together with the idea that different hardware could be used for the same function and that you can create whatever combinations of hardware desired. It would also be possible and streamlined to write new code for this new hardware. The hardware code is split into general scanner, a trigger and a triggered counter. The schematic in Figure 3.2 outlines the timing process. When a scan is initialised in QUDI, a trigger would cause the general scanner to start scanning while simultaneously causing the triggered counter to start counting, ensuring the scanning and counter are synchronised.

The Red Pitaya can be configured to start its outputs when it receives an external digital signal. Similarly, the Swabian Instruments TimeTagger 20 (photon counting hardware) can be preloaded with binwidth information and triggered to start counting photons on an external signal. One of the digital output ports of the Red Pitaya was wired with a fork with one end going in to the digital port allowing external triggering, allowing self external triggering. The other end of the fork goes into the TimeTagger as outlined in Figure 3.6. Now when a signal is sent from from the Red Pitaya, it simultaneously self triggers the scan and the photon counting. Light detected by an Perkin Elmer SPCM-AQR-14 APD causes a signal to the counting channel of the TimeTagger which working in combination with the stage produces a confocal image.

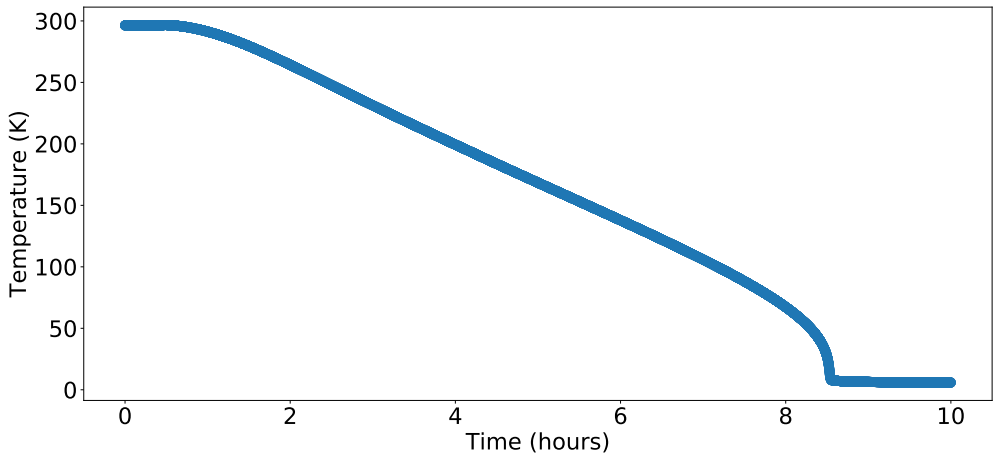

Figure 3.3: **Cryostat cool down.** A typical cool down of the cryostat. The large chamber of the cryostat makes the cooling down a long process on the order of 10 hours.

3.3 Cryostat

The cryostat is a closed cycle Montana Instruments Cryostation s200. It is a convenient automated system that is completely controlled through its software. It provides one-button cooling to the desired set temperature. The software autonomously operates the vacuum pump and helium compressor. There is also a manual mode available if necessary. The cryostat consists of a large chamber where the entire breadboard floor is the cold finger of the cryostat. The breadboard is 190.5 mm in diameter has a grid of M3 holes and essentially behaves like a continuation of the optical table. The vacuum chamber has 7 large 50mm windows for optical access from a large range of incoming angles covering 270^{o}. The chamber is large enough to have multiple set ups running simultaneously, although that has not been pursued in this project. A typical cryostat cool down takes approximately 10 hours and is typically stable within 50 mK.

Figure 3.3 shows a typical cool down event for the cryostat. The process starts with a pump pumping out the air in the chamber until it is below 2 Torr, at which time the compressor starts and cold helium starts flowing through the pipes. At 400 mTorr, the pump turns off. 0.09 mTorr is the pressure gauge limit. Below 30 K the cryostat achieves a high vacuum between 10^{-3} to 10^{-5} mTorr. For measurements at a temperature above 30 K, the cryostat will first cool to below 30 K to achieve the high vacuum before warming up to the desired temperature.

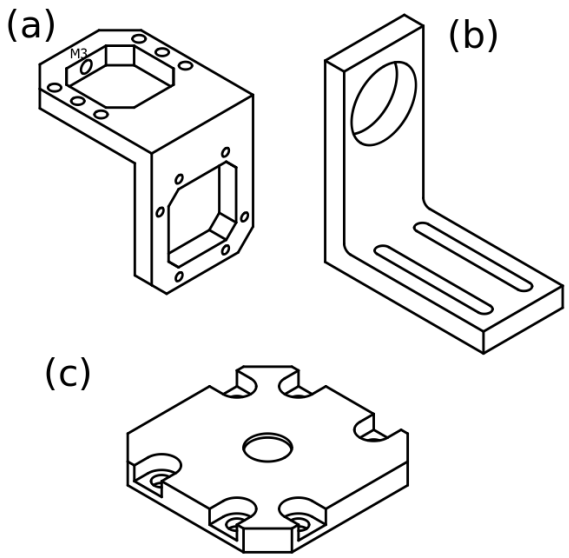

Figure 3.4: **CAD designed positioning parts.** (a) L-bracket that attaches on top of the attocube stack and allows the diamond samples to be mounted vertically. (b) Objective mount that uses the two long horizontal holes to screw into the base of the cryostat as if it were part of the optics table. (c) Sample mount which holds the diamond samples in the shallow circular depression and screws into the L-bracket with a thermal link to the cryostat cold finger in between.

After having the cryostat open for a period of time, such as when swapping diamond samples, it was found that the cryostat would struggle to pump the pressure to below 2 Torr for the compressor to start. This could be circumvented by either manually leaving the pump on for an extended period of time, or by purging the chamber with nitrogen gas. It has been noticed that the pressure of the helium lines appears to be dropping slowly over time, and the lowest possible temperatures are being affected.

3.4 Positioning

Several mounting pieces had to be designed in Computer-Aided Design (CAD) software to mount the diamond samples and the objective inside the cryostat. The parts were made with ultra low oxygen copper, ensuring high thermal conductivity.

The three parts are shown in Figure 3.4. **L-bracket** - This mounts on top of the attocube stack via 6 M2 screws. It extends down the side of the attocube stack, allowing for full XYZ positioning control that an attocube stack offers while allowing all the optics to be kept in

the horizontal plane. It has 6 tapped M2 holes down its side that allow both a thermal link from the cryostat cold plate and the sample mount to attach to it. Attocube shaped holes were cut out to reduce weight and torque the attocube stack experiences from having various pieces hanging over its side. A M3 hole on the top side of the L-bracket was designed so that an M3 screw could be placed through it, pointing the opposite direction than the L-bracket overhangs. This could be used to reduce the torque experienced by the attocube stack. Macquarie Engineering & Technical Services, who cut the copper into the pieces, forgot to include this. **Objective holder** - The base of our cryostat has a grid of M3 holes which have been utilised to hold the objective. The two long horizontal holes in the objective holder provide generous forwards and backwards positioning of the objective. It is fitted with the standard royal microscope society thread, fitting our objective. **Sample mount** - Screws into the front of the L-bracket with a thermal link from the cold finger of the cryostat sandwiched in between. The small circular depression is cut in so a bulk diamond with nanodiamonds on the surface can be pressed into the depression with indium to keep it in place and act as a better thermal contact than air.

The precise positioning of the sample is done via an attocube stack of inertial piezo driven positioners. An ANPz102 scanner attocube sits on the bottom of the attocube stack, giving 5 mm of course positioning in the z (optical y) direction. Two ANPx101 scanners sit on top, rotated at 90^{o} to each other. They give us ±2.5 mm in the x, y (optical x, z) directions. Together they give course motion in x,y,z. This allows positioning inside the cryostat at low temperatures and regions of interest on samples to be found. Figure 3.5 shows the set up inside the cryostat.

The long term solution with this cryostat is to use diamonds pressed into indium, which gives it mechanical attachment to the sample holder with high thermal conductivity, on the front of the sample holder. During this research, we did not quite get to this point and used some quicker methods to mount samples and test the system. The first attempt was to use carbon tape to stick samples grown on silicon substrates on to the sample mount. Somewhere between 290 K and 5 K, we discovered that the glue fails - a lesson learnt the slow way.

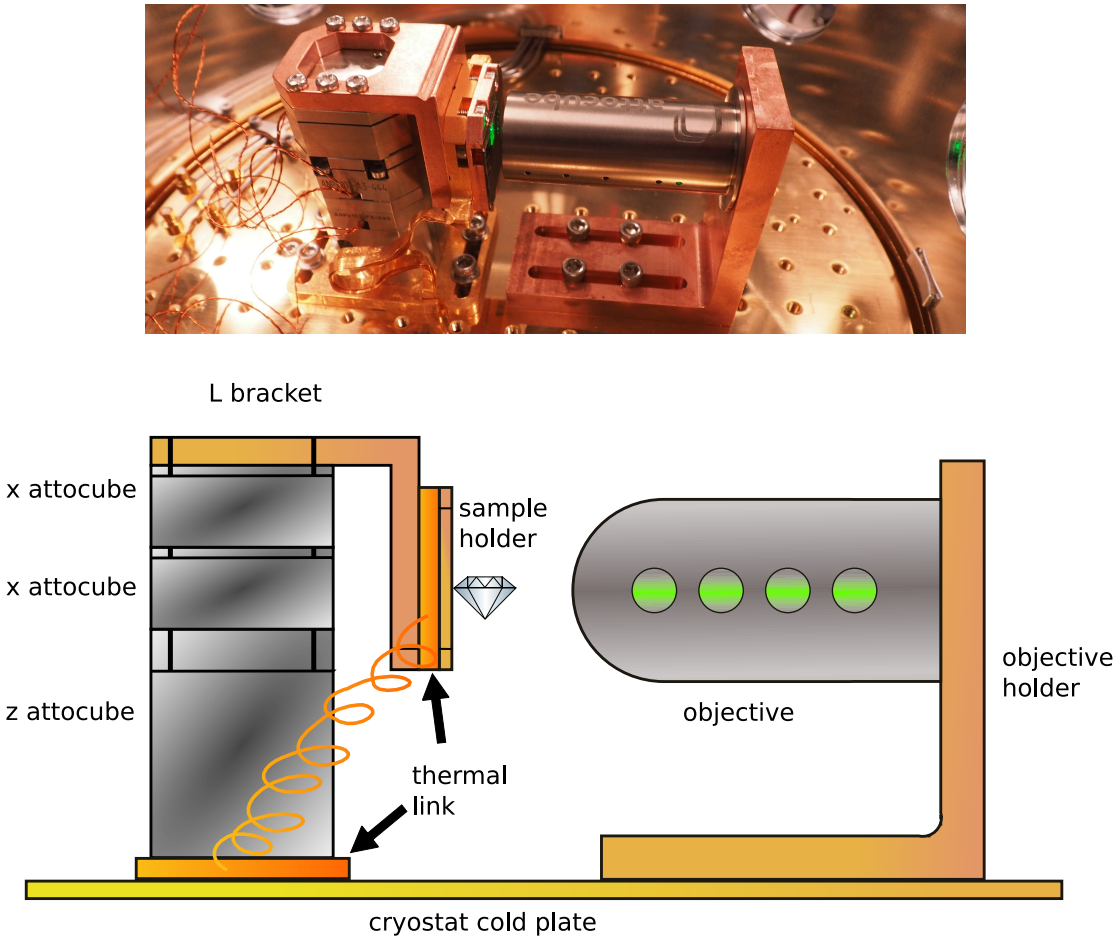

Figure 3.5: **Sample positioning set up.** The objective holder is mounted into the base of the cryostat. An attocube stack is used to precisely position the sample. An L-bracket is used to keep the laser in the horizontal plane. A thermal link between the cryostat cold plate and the sample helps achieve low temperatures at the diamonds.

3.5 Testing

Some of the first tests done were continuous driving of the mirrors with the Red Pitaya. When scanning at kilohertz speeds for a prolonged period of time, the mirrors get very hot, much above the max operating temperature of 50 ^{o}C, but at the hundreds of hertz level, the mirrors run indefinitely while the temperature remains optimal. The servo board driving the mirrors is mounted on the inside of an aluminium case. To dissipate heat, a bridge between the servo and a CPU heat sink was mounted in the case.

Red Pitaya has two key hardware limitations that affects its job to do confocal scanning. 1) It is slow at processing multiple inputs in quick succession. This affects the speed we can scan lines, much slower than the hundreds of hertz speed allowed by the temperature test.

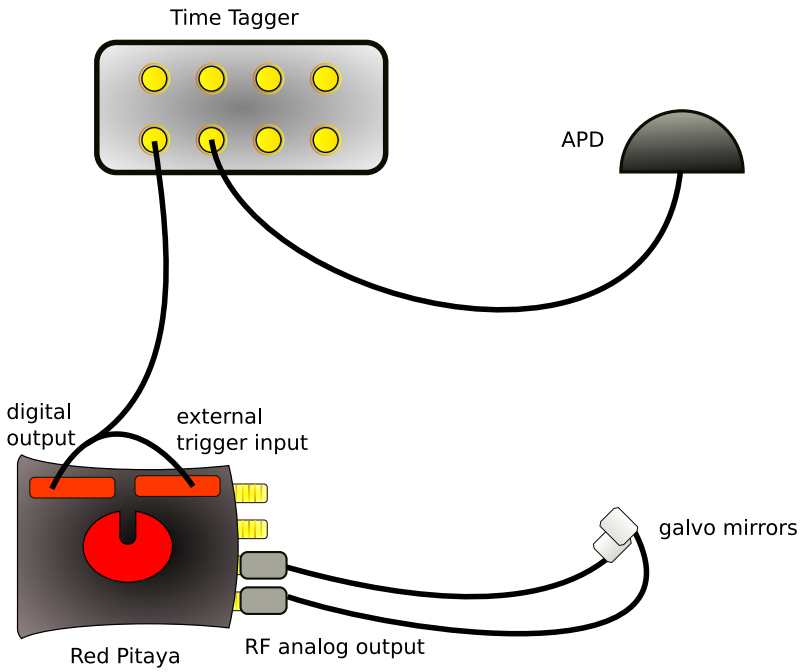

Figure 3.6: **Synchronised scanning and counting.** The Red Pitaya sends out a digital output, simultaneously triggering both the analog outputs of the Red Pitaya to scan and to tell the Time Tagger to listen to counts. The Red Pitaya analog outputs drive the galvanometer mirrors to scan and the Time Tagger counts photons detected by the APD.

And 2) it is very slow to write outputs to the Red Pitaya. This means scanning different lines is a very slow process and any chance to repeated scan the same line should be abused.

It was noticed that even though the cryostat is supposed to have minimal vibrations, there were less fluctuations in counts when centred on a diamond when the cryostat was in standby mode. Standby mode is a low power mode used to keep the chamber relatively cold but with far less thermal stability. This suggests that the increased vibrations between standby and cool-down mode caused the sample to move enough that it was difficult to remain stationary on the diamond.

To time synchronise the scanning of a line with the counting of photons, it is best for these two events to have the same trigger. The TimeTagger and the Red Pitaya can both be set up to perform their actions by an external, digital trigger to a specific input. The Red Pitaya has many digital outputs and therefore can serve as its own ‘external‘ trigger. Figure 3.6 shows how the Red Pitaya is wired into itself to serve as its own external trigger, with the same wire going to the TimeTagger to trigger counting.

This setup is not without its own quirks and testing of synchronisation of laser scanning

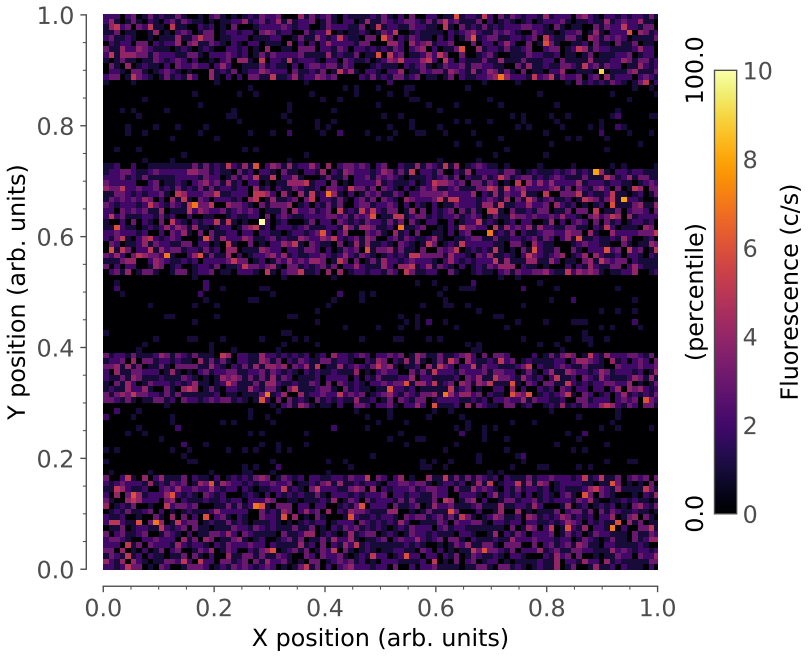

Figure 3.7: **Vertical synchronisation testing.** Background counts during a scan as room lights were switched on and off. Lower counts are clearly seen when the room lights are off, demonstrating vertical counting synchronisation.

and photon counting had to be performed. The simplest test is that over vertical timing. Without any signal to the APD, just measuring background counts. Nearby room lights were switched on and off during a 'scan'. Figure 3.7 shows how the counts varied as the light were flicked on and off, demonstrating that vertical synchronisation is achieved.

Speed tests were performed by placing an Allen key in the centre of the of 4f lens set up. 'Scans' were performed and the Allen key blocks the laser in the middle of the scan. As scan speed is increased, the Red Pitaya is unable to register inputs fast enough to perform each scan and data is missed as can be seen in Figure 3.8. The outline of the Allen key is clearly visible, indicating the ability to do time synchronised scanning. Even though data is missing in faster scans, the time synchronisation is still intact, as the outline of the Allen key is still clearly visible. If the Red Pitaya were capable of registering inputs faster it may be possible for scans to be significantly sped up, but signal to noise ratios start to play a problem.

The confocal set up is incredibly spatially stable, even at room temperatures. A bright, isolated diamond was selected as a suitable diamond for over the weekend drift tracking. Qudi optimised on it every minute by fitting a Gaussian to its fluoresence intensity profile for a total of 62.7 hours, tracking its position. Figure 3.10 shows the stability of the confocal.

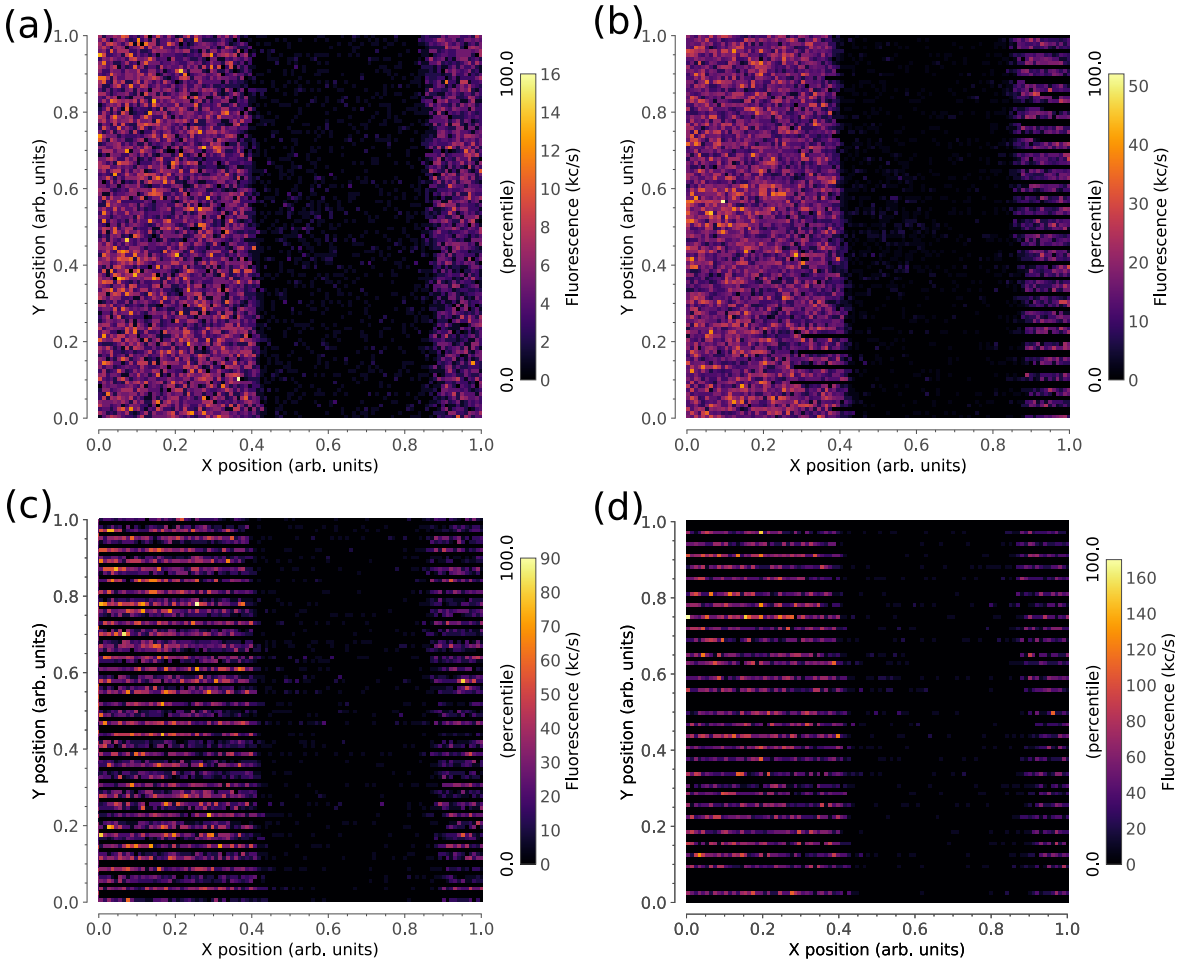

Figure 3.8: **Shadow puppet testing.** An Allen key was placed in the middle of the 4f lens arrangement and the scanning speed was varied. Low counts represent where the Allen key is blocking the laser. (a) 15 lines/s. (b) 20 lines/s. (c) 50 lines/s. (d) 100 lines/s. This figure shows how scanning too fast causes timing issues. Note that the distortions come in the form of skipping scan-lines rather than totally distorting the image.

Over more than 62 hours, the sample drifted less than a remarkable 100 nm and 60 nm in the y and x directions, respectively. This is smaller than the typical size of the diamonds imaged, making it ideal for long, multi-day experiments. It also makes it ideal for taking spectra measurements as you can reliably trust that will be no appreciable drift of the course of a couple hours when taking spectra, meaning you don't need to regularly update the position of the diamonds by switching back to the APD for confocal images. Over shorter time scales, there is about a 20 nm position variation in the drift data. This is largely due to fitting noise when trying to fit a Gaussian to the signal intensity.

The scan range of a galvanometer confocal microscope is determined by the optics

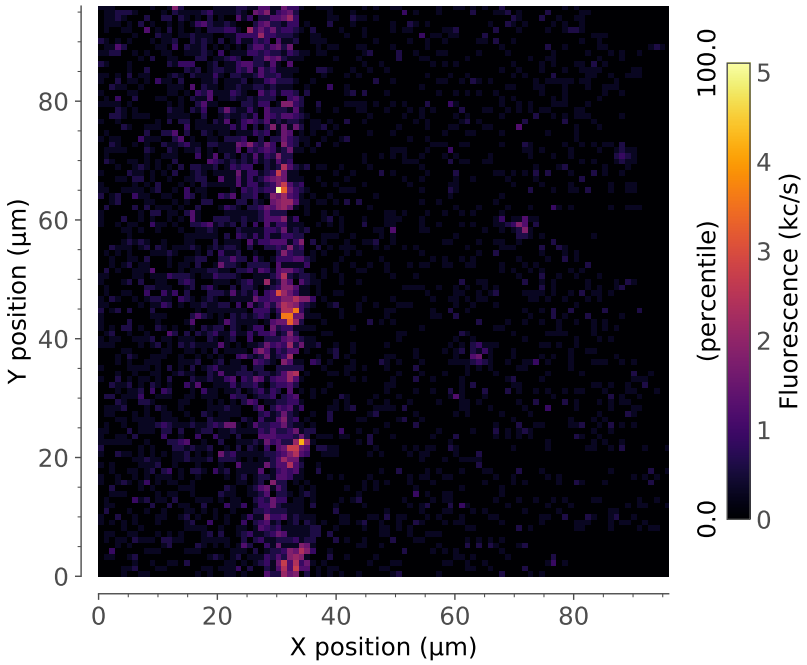

Figure 3.9: **First confocal image.** The first confocal image taken with the confocal microscope of the edge of a silicon wafer substrate diamond sample. The bright vertical line represents the edge of the substrate with the substrate on the right. The bright spots are fluorescing materials, mostly nanodiamonds.

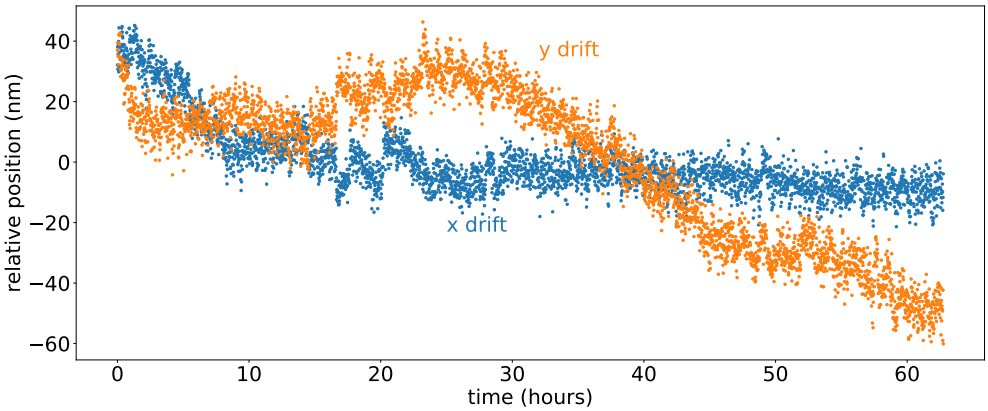

Figure 3.10: **Stability.** The ultra high stage stability is displayed by the less than 100 nm drift in both x and y in almost 63 hours of position tracking.

involved and is not easy to know using geometry. The most reliable way is to scan something of known size and extracting scale from that. Initial estimates of the scan range were given by looking at large, bright nanodiamonds that were scanned using a stage driven confocal. Typical diamonds on this sample were on the order of 1 μm. When looked at with the cryostat confocal, typical diamonds seen took up slightly less than 10% of the image. This gave an estimate of about a 10x10 μm^2 scan range. It was a surprise when scanning another sample where there were scanning electron microscope (SEM) images with a known scale on it. Using this scale the confocal has slightly under 100x100 μm^2 range. The discrepancy may be caused by the low efficiency of the confocal. The diamonds that showed up the most clearly on the scans may have been larger than the typical diamonds seen elsewhere.

This sample has a variety of markers etched into it. Near the centre of where the majority of these markers are located is a large 'blob'. The rough position of the markers was located using an optical microscope where they are clearly visible. To find this location the sample was purposely placed above where the objective was imaging. The back reflection of the confocal was observed while the sample was slowly located using the stepping feature of the attocube stack. When the back reflection went out of focus, it could be easily determined there was some feature on the surface. The sample was continued down and the focus came back. The sample was continued down until we saw a strip that looked like one of the markers that continued right to the sample edge. The green notch filter in front of the fibre was removed and the z positioning was focused on the green back scatter. This gave a clear image of the markers on the surface.

Figure 3.11 (a) and (b) shows the same region of the sample with many clear visible, visually distinct markers. The two images were opened in Inkscape side by side and then overlaid over the top of each other. The SEM image was rotated and adjusted in size such that the markers matched as can be seen in Figure 3.11 (c). This sets the scale for the confocal image. The 20 μm scale bar, which is now 20 microns in both the SEM and confocal images, was repeated until it took up more than the length of the confocal scan at 100 μm. The ratio between the number of pixels taken up by the extended scale bar and the confocal scan multiplied by the 100 μm of the scale bar found the confocal image to be approximately 96 μm in range.

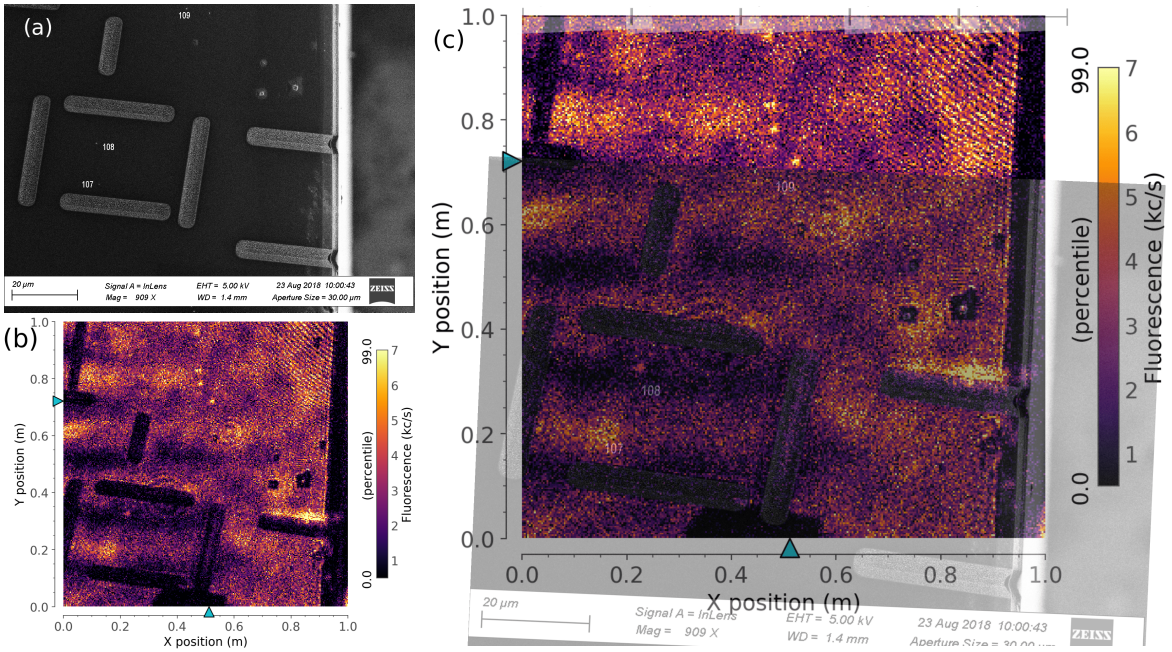

Figure 3.11: **SEM - confocal.** (a) Calibrated SEM image of a silicon substrate sample. Distinct markers are visible as well as some nanodiamonds and the edge of the substrate. (b) An uncalibrated confocal scan of the same region optimised on the back scatter from the substrate. (C) The SEM image overlaid on top of the confocal scan which was used to extract confocal scan ranges.

3.6 Spectrometer

The spectrometer used for measurements in this thesis was the RHEA single-mode spectrograph developed by colleagues working on astronomy instrumentation at Macquarie University [45]. It is extraordinary and unconventional, taking parts of the spectrum that would be outside of the CCD image and wrapping them back as different orders in the CCD image. This gives an outstanding wavelength range at high resolution. However, being essentially a prototype device the spectrometer presented two key challenges to overcome. When the optics wraps different parts of the spectrum back on the CCD image, there is some spectral overlap between the orders. The CCD image is more sensitive towards the centre of the orders than the edges, requiring a per-order amplitude correction factor. There is also sensitivity variance between the orders themselves. The amount of overlap in the orders was determined by using a tuneable white-light laser (NKT Photonics SuperK Extreme with SuperK Select+ filtering head). The laser was varied across a number of wavelengths to provide spectral peaks that allowed determination of the RHEA order overlaps. The variance in intensity was

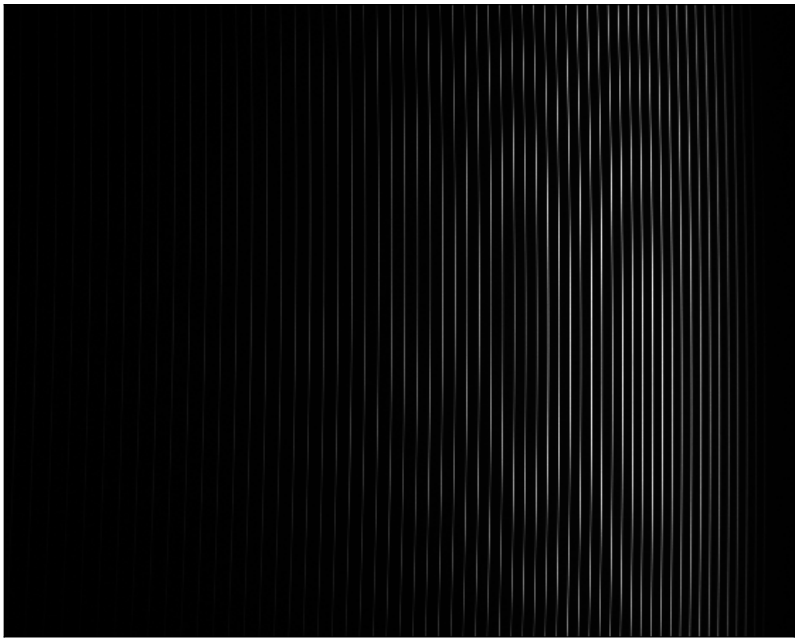

Figure 3.12: **White light source on CCD.** The raw CCD image of the white light source of a tungsten bulb. Each vertical lines represents one wavelength order. Wavelength increases travelling up the CCD image, along an order and by travelling right along the orders.

calibrated by exposing the spectrometer to a white light tungsten source. Figure 3.12 shows the CCD image taken from the tungsten bulb. The known intensity of the this spectrum was used as an amplitude correction factor. The simultaneous wide range and high resolution of this spectrometer meant that each spectrum contained a large amount of data that required detailed investigation for spectral features outside the initial wavelength-band of interest.

The juvenile sea squirt wanders through the sea searching for a suitable rock or hunk of coral to cling to and make its home for life. For this task, it has a rudimentary nervous system. When it finds its spot and takes root, it doesn't need its brain anymore, so it eats it! It's rather like getting tenure.

Daniel C. Dennett

4

Characterising nanodiamond samples

Various nanodiamond samples were investigated to characterise the confocal and the cryostat. Narrowing of the linewidths due to reduced thermal broadening is observed. Understanding how the strain distribution in nanodiamonds varies with fluorescence brightness is attempted. Temperature variance in nanodiamonds due to how thermal contact the sample holder is made is explored ,both on the same substrate and comparing between substrates. Characterising samples is important for many future research directions. Superradiance measurements require homogeneous strain environments and small crystal sizes for indistinguishability. Thermal broadening washes out all sharp features so that these characteristics can only be seen at low temperatures. The QMAPP group is now capable of answering these questions.

4.1 Nanodiamond samples

Chemical vapour deposition (CVD) growth of diamond allows for high level of control of the growth process. It involves lower pressures than other diamond growth techniques.

The diamond samples studied in this chapter were grown in the QMAPP group, but that fabrication work was outside the scope of this research project. CVD growth was performed by Dr Fabio Isa, a postdoctoral fellow with a joint appointment at the Materials Division of CSIRO. In order to produce samples with high concentrations of certain colour centres, Dr Isa is working to grow nanodiamonds directly on substrates that provide the dopants. Three different samples were provided to characterise and examine the low temperature properties.

The first sample was a pure Si substrate on which diamonds on the order of 1 μm had been grown. This sample was intended to have high concentrations of SiV incorporated during growth, as the growth plasma is known to etch the Si from the substrate [23]. The large size of the diamonds (for nanodiamonds) was to allow plasma conditions to be checked and optimised for single-crystal growth. This sample did not have any focused ion beam (FIB) markers. For simplicity throughout this thesis, this sample is referred to as "Sample Si".

The second sample was a thin SiGe layer sitting on top of a much thicker pure Si base layer. The CVD-grown nanodiamonds on this sample were expected to have high densities of SiV and GeV centres as a result of some of the substrate getting incorporated to the diamonds in the growth process. FIB markers were made on this sample after the PL measurements reported in this thesis. Here this sample is labelled "Sample SiGe".

The last sample was a thin layer of pure Ge sitting on top of a similar pure Si base layer as sample SiGe. Here this sample is called "Sample Ge". Sample Ge was used for scan range calibrated outlined in the previous chapter.

4.2 SEM imaging and marker etching

Being able to repeatedly locate regions of interest is valuable for studying individual diamonds at multiple temperatures, across different experiments, in different experimental set ups and over the course of months and years. To reliably do this you need points of reference. A SEM was used to identify regions of the substrate with promising diamonds, and markers were etched into the substrate using FIB milling. Areas with interesting diamonds were found by using the SEM at low magnifications as the edges of the sample were swept over. Areas close to the edge of the substrate are preferred as they are much easier to relocate in a confocal scan. This is exacerbated since the scanning speed of the confocal is significantly slower than the SEM. Areas where the substrate is clear and where visually distinguishable but high

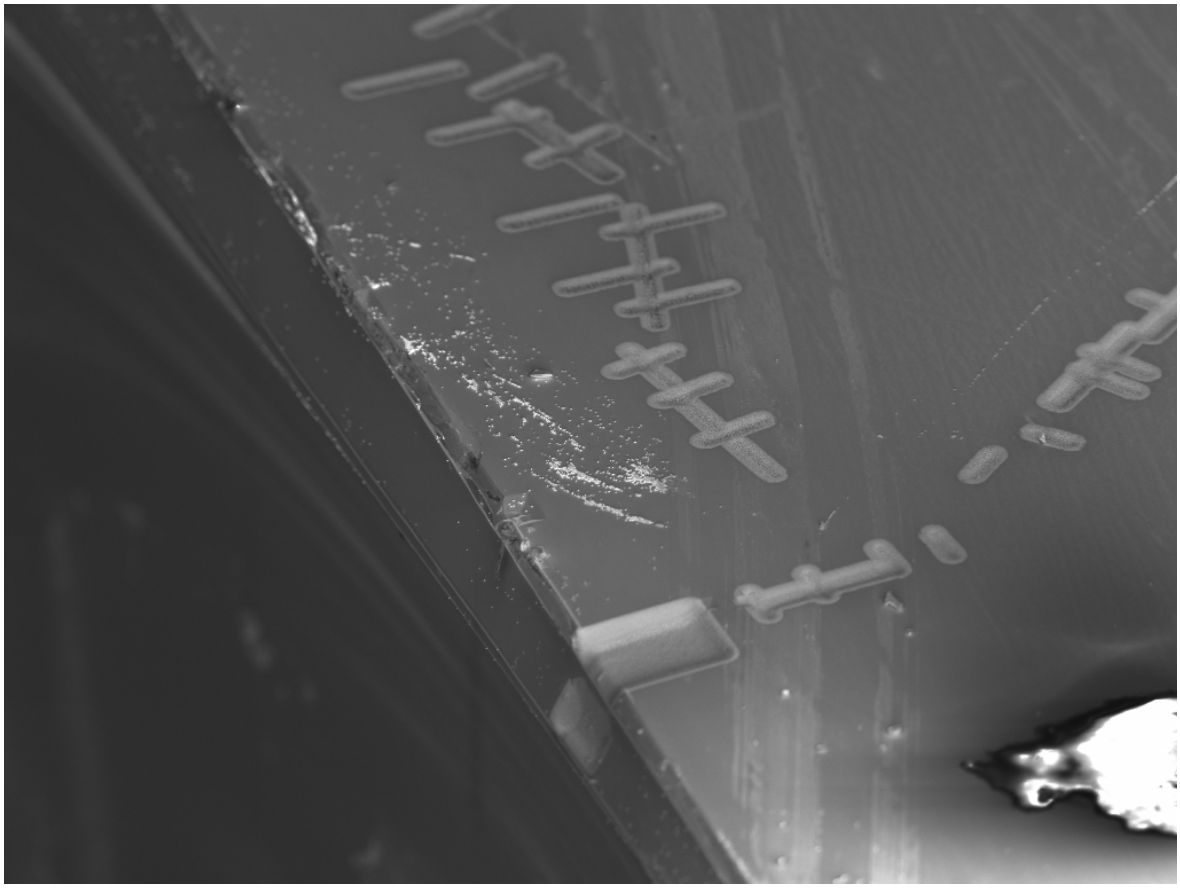

Figure 4.1: **Markers etched into substrate**. Angled SEM image of diamond samples, showing markers etched by FIB milling.

concentration of nanodiamonds are preferred regions of interest.

Once a number of areas of interest were located with the SEM, FIB markers had to be strategically placed so that they could be utilised in confocal imaging. FIB markers were made by blasting the substrate with a gallium beam for predefined times and over specified shapes. The first thing to consider is how far from the edge of the substrate the regions are. There must be a continuous chain of identifiable markers from the edge within one scan range of each other so there is little chance of finding yourself in-between markers and uncertain of your position. FIB markers cannot be made too close to the diamonds themselves as there is a risk of diamonds being in the blast zone.

Figure 4.1 Shows an angled overall view of a number of regions of interest taken with an SEM. There exists a large, rectangular FIB marker overhanging the edge of the substrate. This is significantly deeper than the rest of the FIB markers and was made to appear very obviously on confocal scans for easy initial orientation. Attempts to keep FIB markers as distinct as possible were made.

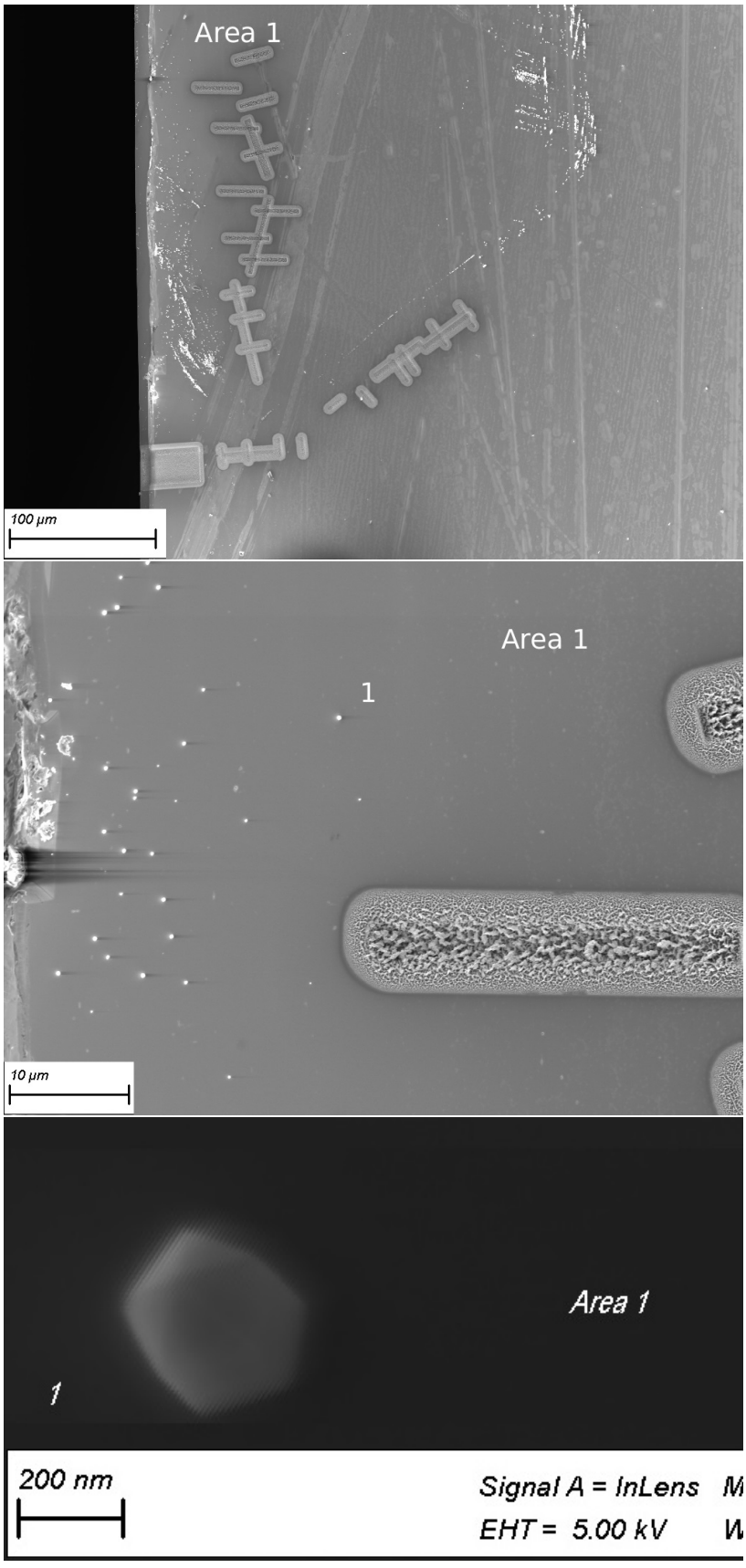

Figure 4.2: **FIB mapping SEM image** SEM images of Sample SiGe at at varying magnifications, showing FIB markers and nanodiamonds

4.3 Fluorescence microscopy

In separate experiments, the three samples were mounted inside the cryostat for PL measurements. Each sample was mounted to the front of the sample holder by clamping them in place. The main problem was that it was a single clamp. Using more clamps would have obstructed the approach of the objective. This is not the desired long term solution as it causes poorer thermal contact than being pressed into the sample holder with indium and lower temperatures at the diamonds are harder to achieve as a result. However, it was necessary as a quick and easy stopgap for the short time frame that was given. Fluorescence images were recorded with the APD measuring photons filtered through a 550nm long-pass filter. The photoluminescence intensity was not saturated.

Sample Si was mounted first and used to confirm the ability to do fluorescence microscopy. It was the ideal sample for confocal characterisation as the diamonds are large, bright and formed in high density regions. Once the ability to do quality PL measurements was confirmed, we sent those bad boys cold.

The diamonds were bright, had large amounts of SiV centres that showed a variety of strain environments. Spectra were taken for 23 diamonds with the cryostat at 8 K, 13 diamonds at 70 K, 2 diamonds at 140 K and 11 diamonds at 300 K.

There are no FIB markers on this sample as it wasn't originally intended to have interesting features. Regions of interest were found by moving along the edge of a sample until nice fluorescence spots came into view. It is not reasonably possible to go back and find any of the regions of interest due to the lack of FIB markers and trying to keep track of diamonds during cool-down and warm-ups is difficult. It can only be done when varying temperature slowly. It was desirable to have a modest set of data from the same diamonds at various temperatures. The diamonds that were imaged at 8 K and 70 K were lost to drift when going from 70 – 140 K and dreams were crushed. The diamonds imaged at 140 K and 300 K were not related to each other or the colder diamond set.

Sample SiGe was mounted next. An absolute point of reference was wanted so dreams could not be crushed so easily. This was before FIB markers were made on the substrate so it was mounted to look at a corner to be the absolute reference. A handful of diamonds were found on this corner and none of them had any evidence of germanium-vacancy centres, although they were fluorescent with SiV centres. The sample was rotated so that another corner was imaged, this corner had more diamonds but again none of them exhibited signs

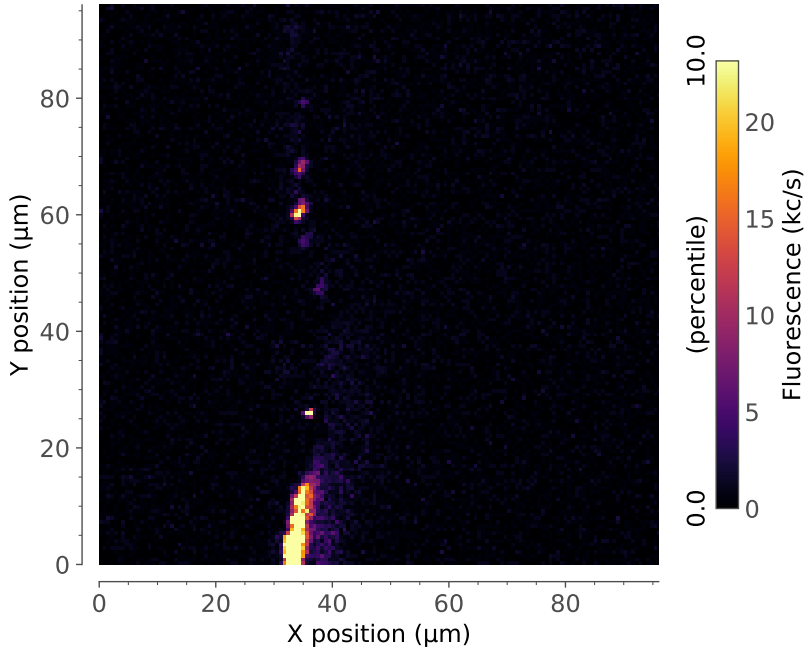

Figure 4.3: **Diamond sample region of interest.** A typical confocal scan showing a high density of nanodiamonds on the edge of the substrate of sample Si.

of GeV. As there was already data from SiV centres, it was decided not to cool-down to look at spectra and only room temperature measurements were made. The spectra were similar to those from the other samples and are not presented in this thesis.

Sample Ge had extensive FIB markers in areas that were known to have many diamonds and allowed for the determination of the scan range. The FIB markers were found in confocal scanning and PL measurements were able to be made on diamonds that also had SEM images. A whopping 59 diamonds were examined at 6 K and 32 at room temperature, and these were known from SEM imaging to be on the order of 250 nm. There was a surprisingly large amount SiV centres clearly visible in the spectra. In addition to this, many unknown peaks were found in the spectra in a large amount of the diamonds that could represent unknown colour centres.

4.4 PL spectroscopy for temperature characterisation

While the cryostat can reliably achieve low, stable temperatures, there is an unknown element for how cold the nanodiamonds themselves get. The diamonds have several interfaces between them and the cold finger , attached to a 550 μm thick Si substrate (and an additional thin layer

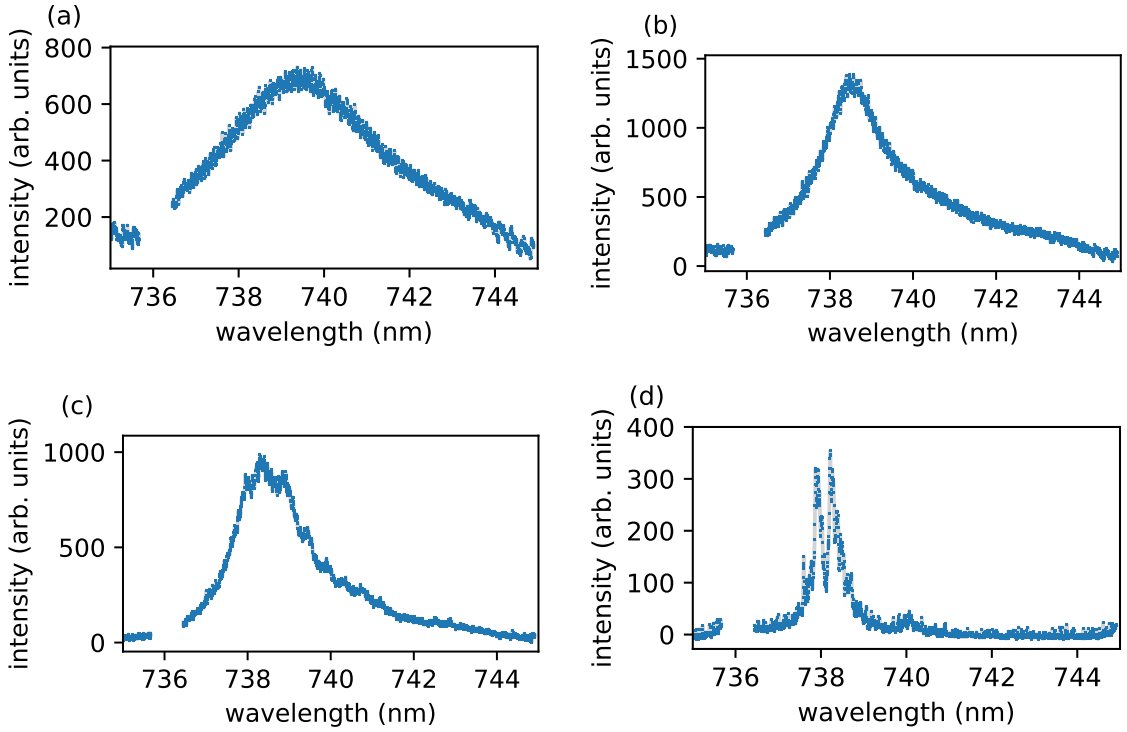

Figure 4.4: **Silicon vacancy temperature variation.** Typical spectra of diamonds on Sample Si at (a) 300 K. (b) 140 K. (c) 70 K. (d) 8 K. As the temperature of the diamonds drops down from room temperature, the distribution width shrinks. As the temperature gets towards 70 K, some individual features become visible. These features become very sharp and individual fine structure lines of the ZPL become distinct. Missing spectra around 736 nm represents data missing from the spectrometer due to non-overlapping orders.

in the case of samples SiGe/Si) which is not optimal for thermal contact. PL spectroscopy can give some estimates for the actual temperature of the diamonds, providing information about the thermal contact between the nanodiamonds and the substrate.

Figure 4.4 shows how ensemble SiV spectra typically vary with temperature. At room temperature, the spectrum is quite broad from both the inhomogenous and thermal broadening. As the diamonds cool down, the thermal broadening narrows the spectrum until sharp features start appearing as individual ZPL transitions start to dominate parts of the spectrum. The average FWHM at 300 K was found to be 5.8 nm. At 70 K, the average FWHM has dropped to 1.9 nm and this remains constant until down to 8 K. While these spectra linewidths are not taken of the same diamonds, they are randomly selected and should represent the diamonds on Sample Si. At very low temperatures, single ZPL transitions are visible as the thermal broadening is much less than the inhomogenous broadening in this sample. The

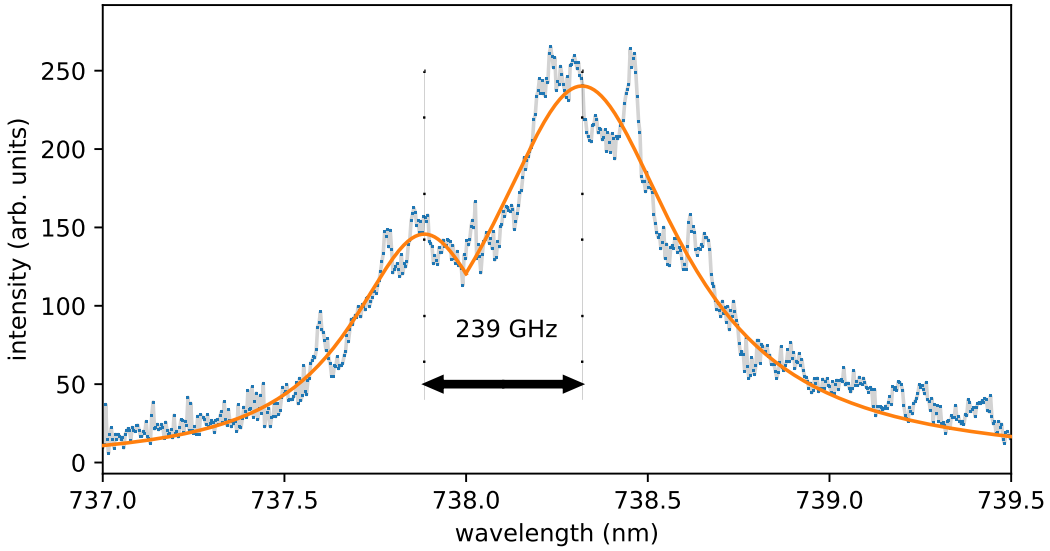

Figure 4.5: **SiV centre excited state splitting.** The spectra of a SiV centre where the splitting between the excited state is producing a two peak structure.

broadening visible is from the ensemble inhomogeneous broadening in which spectra from SiV centres seeing varying strain environments partially overlap.

Figure 4.8 shows the temperature variation from a single nanodiamond on sample Si. Peaks that are starting to become visible at 70 K become sharp at 8 K. Peaks that were not visible from thermal broadening at longer wavelengths have become visible. The intensity of the diamond at higher temperature is significantly lower. This was observed across all the diamonds and is the expected behaviour.

No single site SiV centres were found in any of the diamonds. This makes it difficult but not impossible to look at the excited state splitting. Diamonds with low or homogeneous strain distributions can still have resolvable splitting. Observing ground state splitting would not be possible in samples of the nature looked at in this thesis. Figure 4.5 shows the SiV ZPL spectrum of a nanodiamond fitted with two lorenztians. It was located on sample Si and is the narrowest distribution diamond looked at with a FWHM of 0.80 nm. There are two clear peaks in the data, each fitted with a lorentzian. The separation between these two peaks likely represent the excited state splitting in SiV centres as the two fitted peaks are split by 239 GHz, very close to the expected 258 GHz value.

At low temperature, the probability of the SiV centre existing in the +1 and -1 orbital states of the excited state is given by the Boltzmann distributions. Therefore, the ratio between the

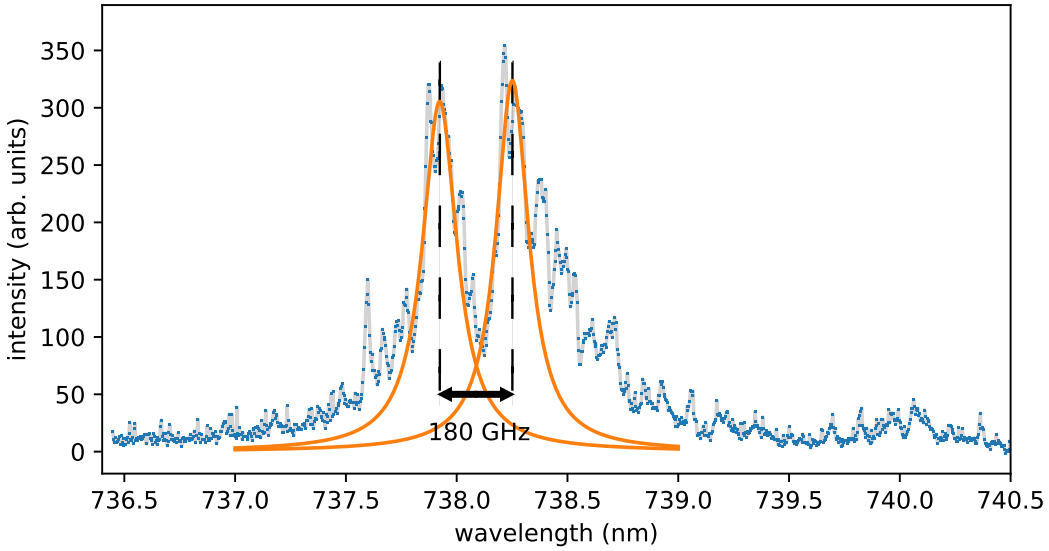

Figure 4.6: **Low strain diamond separation.** The second lowest strained diamond looked at with a FWHM of the full distribution of 0.81 nm. The distribution is dominated by two peaks with a separation of 182 GHz (0.33 nm) and may represent the excited state splitting of a SiV centre.

emission intensity of the +1 and -1 levels of the excited state is given by ratio of the respective Boltzmann distributions.

$$r = \mathrm{e}^{-\frac{dE}{kT}}$$

Where r is the ratio between the intensities, dE is the difference in energies, k is Boltzmann's constant and T is temperature. As the two distributions are approximately equal in width, the ratio of the distribution heights is approximately the ratio of the intensities. The heights of the peaks is taken as the heights of the two Lorenztian peaks. The ratio is 0.607 which gives a temperature estimate of 23 K. This is a reasonable estimate for an 8 K cold finger and the previously mentioned difficulties involving thermal contact of nanodiamonds.

The spectrum another sample Si diamond that is shown in Figure 4.6 has a FWHM of 0.81 nm and is the second lowest distribution linewidth found, making it another strong candidate for looking at excited state splitting. In this case, the Lorenztian fit of the lower energy (higher wavelength) level of the excited state does not capture the intensity as it is not a symmetric distribution and so the fit misses much of spectrum. The relative heights of the fits is similar but the lower energy distribution hides much of its intensity in the significantly broader

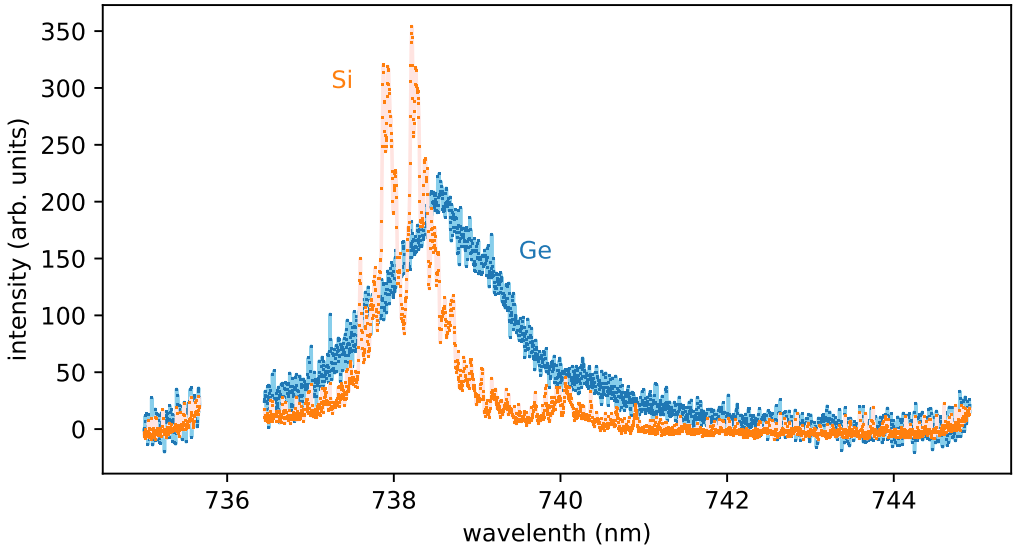

Figure 4.7: **Spectra comparison of samples Si and Ge**. Representative SiV spectra from two samples, one on sample Si and one on sample Ge. Despite having the cryostat at similar temperatures during spectra measurements, the Ge sample appears to be thermally broadened due to the lack of sharp features.

distribution. To capture the relative intensities then, the areas where the two distributions are clearly separated (to the centre of the respective Lorentzians), the intensities were numerically integrated. From the centre of the distributions through to where the two distributions cross over, the Lorenztian fits were integrated. The ratio is 0.41 and the energy separation is 180 GHz which gives a temperature of about 10 K. This is an implausibly low temperature given the cryostat cold plate was at 8 K and the issues with thermal conductivity. This estimate requires a sharp division in the spectrum between the +1 and -1 energy states. There is some significant overlap in between the two distributions, leading to some double counting intensity which is hindering the ability to do this estimate.

Figure 4.7 shows the low temperature spectra of a diamond from Sample Si and from Sample Ge and are typical representatives from each sample. Both of these diamonds have a similar total brightness (Sample Si intensity is approximately 70% of the Sample Ge diamond), being excited at the same laser power and using the same objective as a part of the same confocal, and therefore presumably have a similar amount of SiV centres in them. However, there is far less fine structure visible in the sample Ge diamond, indicating that it either has a larger inhomogeneous broadening from a larger ensemble, or it is being

thermally broadened. It is unlikely to have a significantly larger ensemble because it has similar brightness, and so it most likely has been thermally broadened. Both samples consist of a 550 μm thick Si(001) substrate P doped at a concentration of 10^{17} cm^{-3}. In addition to this, sample Ge has a 2 μm thick layer of pure Ge. At these cryostat temperatures, Ge has a significantly higher thermal conductivity than silicon. However, the existence of an additional layer might add enough thermal resistance to stop the diamonds from reaching similar temperature. It is hard to imagine such a thin layer of Ge would have such a large impact on temperature. There may be poorer thermal contact between the substrate itself and the sample mount arising from inadvertent inconsistencies between the way each sample is mounted. If this is the case, then the thermal contact achieved is extremely sensitive to minor variations in mounting.

The Sample Ge diamonds might exhibit a greater inhomogenous distribution as seen in comparison of the linewidth distributions in Figure 4.9 (a) and Figure 4.10 (a) which may look like thermal broadening and cause the apparent temperature difference. This is unlikely to fully explain what is seen here as even the extremely low intensity diamonds of Sample Ge do not have any of the sharp features seen in the Sample Si diamonds. The comparison of the samples was made using similar intensity diamonds and it was not possible to directly compare lower intensity spots due to none being seen in the Sample Si.

4.5 Linewidth and ensemble strain

Spectrum linewidth and fluorescence intensity information was gathered to both look for suitable diamonds for other experiments (like superradiance) and to understand the relationship between them. Do the brighter diamonds have a narrower distribution because they are large, single crystal diamonds? Or do they have a broader distribution because they are polycrystalline? Larger nanodiamonds are closer to the bulk diamond limit, exhibiting lower strain. The strain in the individual crystals of a polycrystalline diamond should each exhibit random strain, leading to greater inhomogenous broadening. The linewidths of SiV spectra were calculated by doing a Lorentzian fit on the ensemble distributions. Originally this was done by doing a Gaussian fit but lorentzian gave better fits. However, this had virtually no effect on the shape of the distribution, only the linewdiths were slightly shifted lower with the lorentzian. The intensity was calculated by summing up the intensity for every pixel between

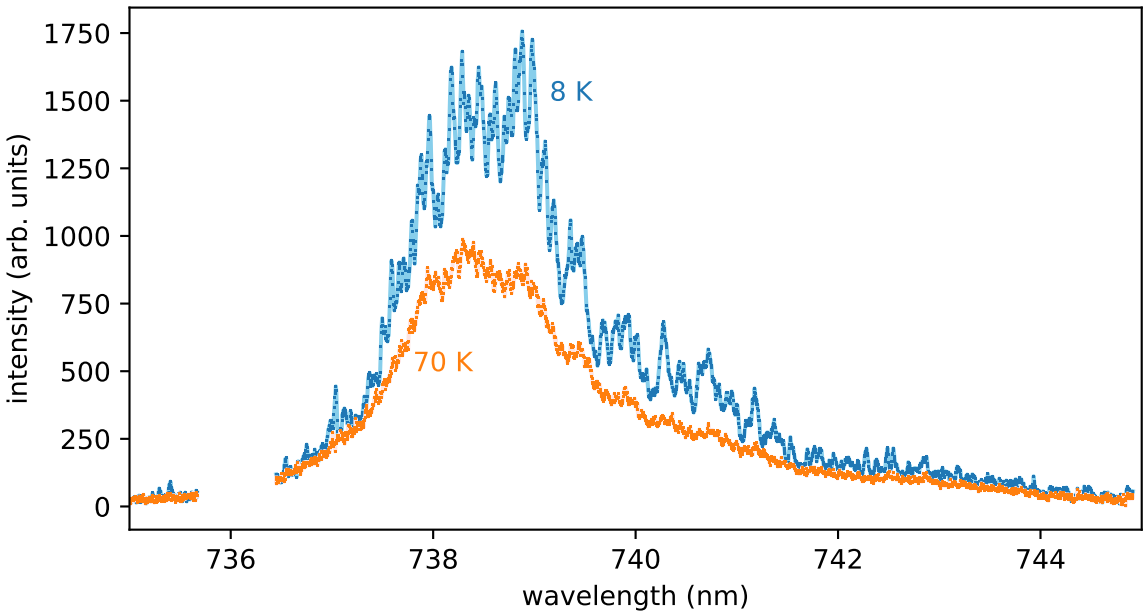

Figure 4.8: **SiV centre temperature spectra variation.** Comparison of spectra of the same nanodiamond at 8 K and 70 K. Sharper features that are thermally broadened at 70 K are resolvable at 8 K. Lower temperature SiV centres have greater fluorescence intensity.

735 – 745 nm.

Figure 4.9 summarises the information on the linewidths and brightness from Sample Si and Figure 4.11 from Sample Ge. There does not appear to be any relationship between the brightness and linewidths from these data. This could mean the brighter diamonds are a combination of large, single crystal and polycrystalline diamonds, but no strong conclusions can be made. The distribution of linewidths are much greater in the Sample Ge diamonds. This is expected from the relative size of the nanodiamonds. Strain is generally higher and less uniform in smaller diamonds, leading to greater linewidths.

To argue that these samples represent a medium size ensemble sample of SiV centres, the sharp, single features seen should be individual transitions of the ZPL. Figure 4.11 shows the ensemble spectra with one of these sharp features highlighted in red. This line was chosen as it was sharp and relatively isolated. While this ensemble is relatively bright, the linewidth is the broadest in the sample and there are many (presumably) individual ZPL transitions visible. Figure 4.11(b) shows a close up of this peak with a Lorentzian fit applied. This gives a linewidth of 0.052 nm (29 GHz). This is much broader than the 100 MHz that the low temperature ZPL should be. This linewidth is close to the instrument limit of the

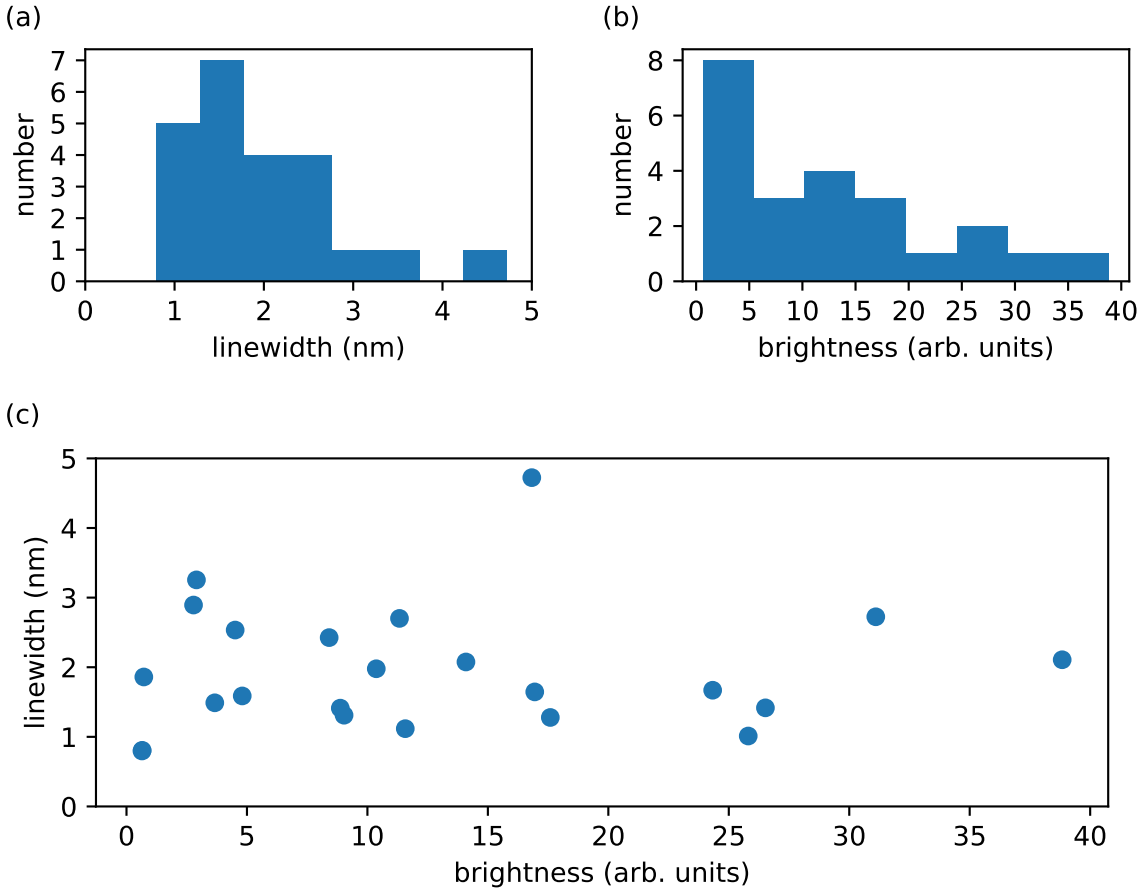

Figure 4.9: **Width v brightness silicon vacancy on sample Si at 8 K.** (a) Histogram of the linewidth of the SiV centres. (b) Histogram of the brightness of the SiV centres. (c) Plot of the linewidth v brightness. No correlation can be seen.

spectrometer at this wavelength, so it is difficult to draw strong conclusions.

4.6 Germanium vacancy and other novel defects

The great surprise of this story is the inability to confidently claim the presence of a GeV centre in any of the diamonds examined. Two of the samples had significant amounts of germanium in the substrate yet it appears that very little got incorporated into the lattice during CVD growth. This suggests that Ge is much harder to incorporate into the diamonds during growth than thought. As part of the sample-growth preliminary characterisation (performed off-campus by Dr Isa), there were spectral features interpreted as GeV spectrum visible during Raman measurements. It was not possible to identify which nanodiamond produced this, and the observation could not be reproduced in confocal measurements. Despite this, we present

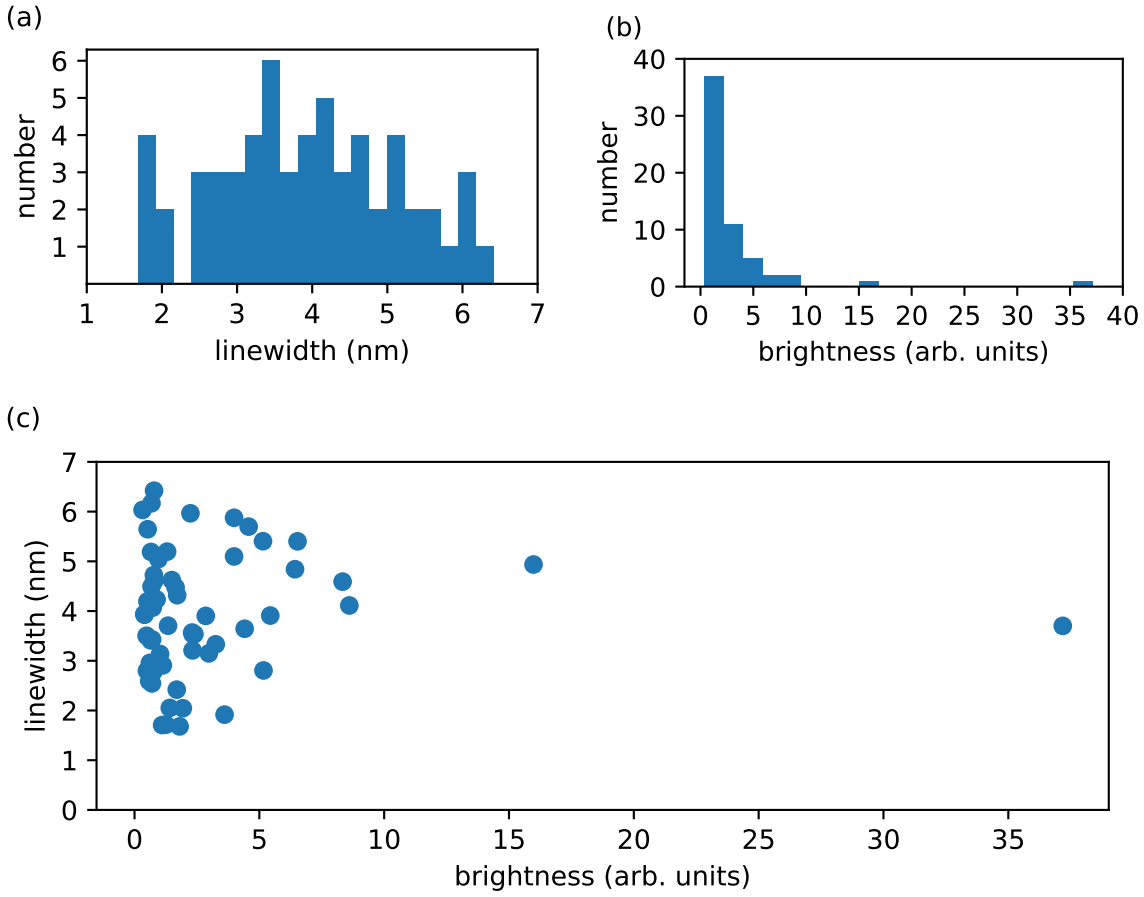

Figure 4.10: **Width v brightness silicon vacancy on Sample Ge at 6 K.** (a) Histogram of the linewidth of the SiV centres. (b) Histogram of the brightness of the SiV centres. (c) Plot of the linewidth v brightness. No correlation can be seen.

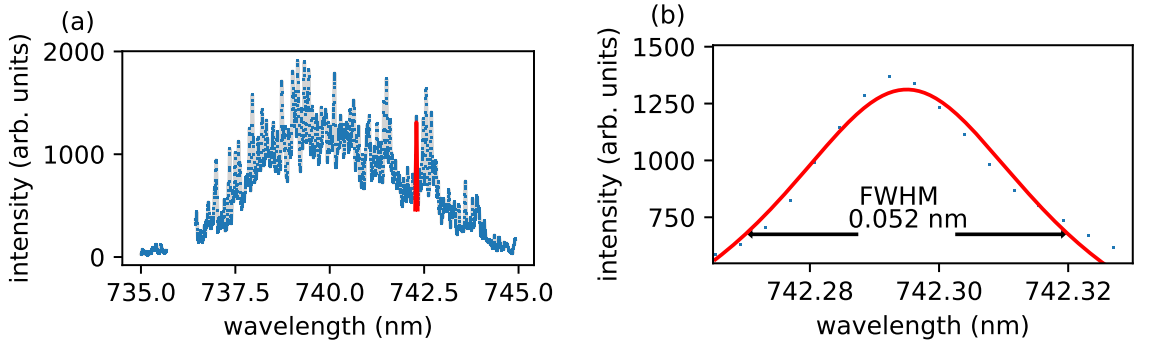

Figure 4.11: **ZPL linewidth.** Left: SiV spectra of a diamonds with many ZPL lines resolvable. In red is a lorentzian fit on one of these transitions. Right: a close up of this transition with the same lorentzian fit.

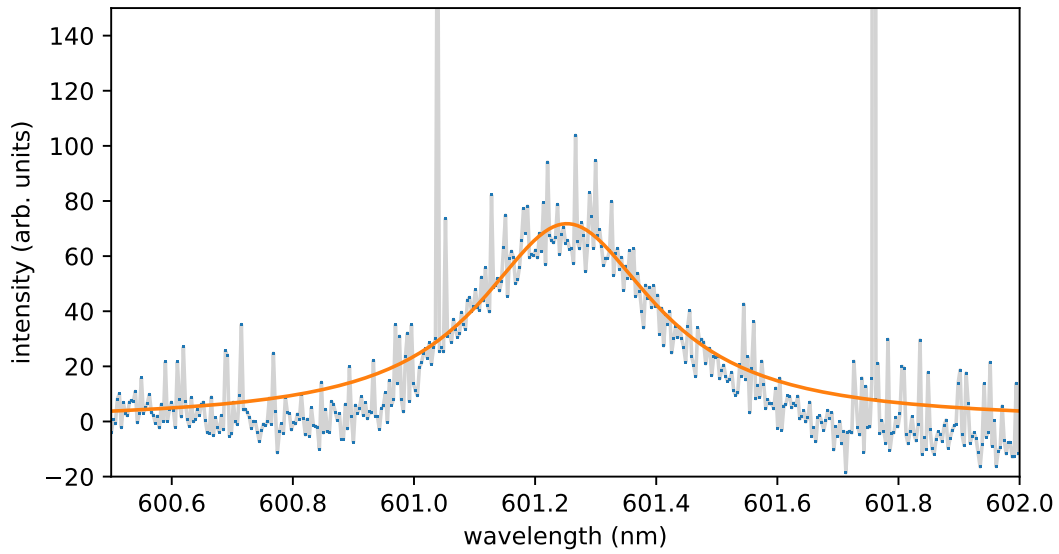

Figure 4.12: **Possible GeV centre.** This peak appearing near where a GeV centre might emit that was found in sample Si. It was not clear enough to allow reliable identification.

some fluorescence which may be from GeV centres.

Despite the expectations of high density of GeV centres in Sample Ge, SiV centres dominated the diamonds with a handful of unknown peaks and only one weak possible candidate for a GeV centre. Si contamination into these diamonds is not too unexpected considering the base of the substrate is pure Si. Because of this, the focus was shifted to characterising the SiV centres in these diamonds and comparing them to the pure Sample Si. The biggest immediate difference was the intensity from photoluminescence measurements. These diamonds are significantly smaller with typical sizes around 250 nm vs the 1 micron of the previous sample. This along with the extra barrier of no Si on the top layer made for significantly lower number of SiV centres.

An interesting peak found in the spectrum of a sample Si diamond is displayed in Figure 4.12. A peak near the GeV ZPL, around 601 nm in what would be be a rather broad FWHM of 0.35 nm (293 GHz) if it were a GeV centre at 8 K cryostat temperature. The most interesting aspect is that this is the only sample which was not expected to contain germanium. The substrate is supposed to be pure Si, but impurities on some level would exist. The level of purity of the substrate is not known but it only takes a single atom to create the defect. Most likely, this peak has another origin.

One of the diamonds in Sample Ge may have a large-strain shifted, thermally broadened

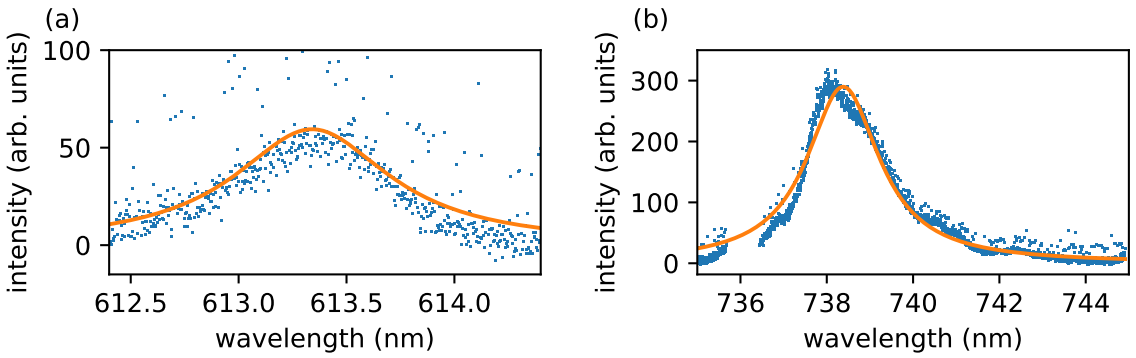

Figure 4.13: **Best GeV candidate.** (a) Unknown peak representing the best candidate for a GeV centre with a Lorentzian fit in orange. (b) SiV spectrum from the same nanodiamond showing relatively low strain.

GeV centre. Figure 4.13 (a) shows an ultra low intensity peak at about 613.5 nm fitted with a Lorentzian function. This peak has a 0.88 nm (702 GHz) FWHM. While it appears likely that the diamonds in this sample are thermally broadened, it is not plausible for this level of broadening. Similarly, for this peak to plausibly be a GeV centre, it would need to be in a large strain environment for it to be shifted this far from 602 nm. Looking at the SiV spectrum in the same diamond can help to understand the strain environment in this diamond. Figure 4.13 (b) shows the SiV spectrum from the same nanodiamond. With a FWHM of 2.05 nm, it is one of the narrowest distributions of any of the diamonds in sample Ge. This suggests that the overall strain of the sample of diamond is quite low. Thus, it is most probable that this peak also does not come from a GeV centre.

Some concerns have been raised about the sensitivity of the spectrometer around the expected unstrained GeV ZPL of 602 nm. The presence of unknown peaks found at 613 nm, 614 nm, 582 nm in sample Ge and 601 nm in sample Si indicate that that there is sufficient sensitivity to detect GeV spectra if present, especially because special attention was paid to this area. An order-overlap of the spectrometer occurs between 604-605 nm, where a moderately strain-shifted GeV ZPL may sit, and it is possible that this could make the detection difficult for a low intensity diamond.

It is disappointing from the QMAPP group perspective that diamonds grown to have large amounts of germanium had no evidence of any GeV. The observation of SiV in the spectrum establishes that the fluorescent spots studied on these substrates are indeed diamond material. The presence of unknown peaks (some of them very low intensity) in the area where GeV

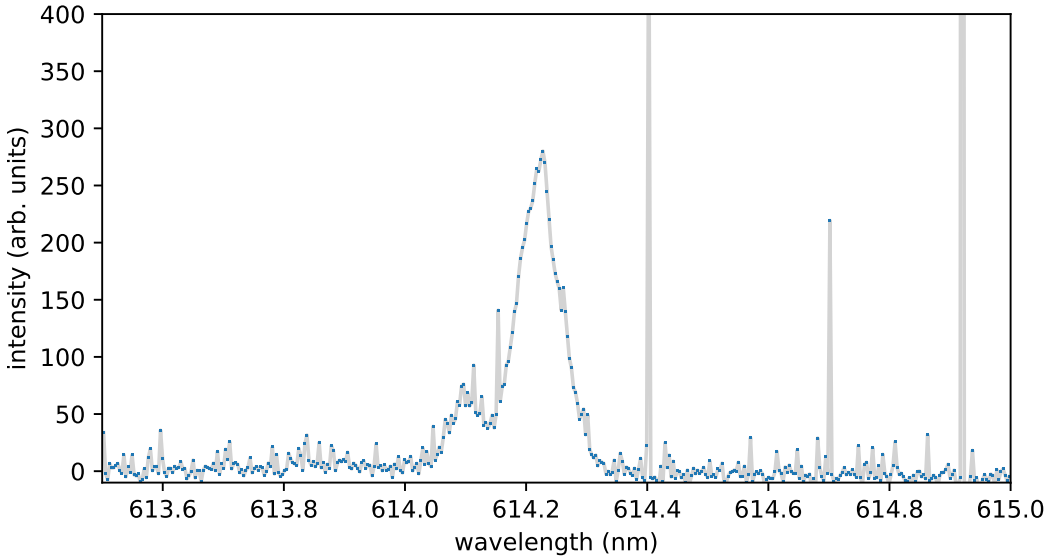

Figure 4.14: **Unknown 614 nm peak.** High resolution spectra over large wavelengths gives the benefit of finding unintended points of interest in the data. This spectra represents possibly an unknown defect in the diamond. Many more features like this were inadvertently found.

would be make it implausible that it could not be detected if it were present in moderate quantities.

The uplifting side of the story is all the unknown and unusual peaks found due to the spectrometer's range. Figure 4.14 shows just one of these unknown peaks found in a diamond on sample Si. This 614 peak could be a little known thallium defect described in Zaitsev book [11]. This thallium defect spectrum consists of split ZPL peak at 614.5 nm accompanied by a broad spectrum with peaks at 658 nm, 660.4 nm, 667 nm and 670. and weak peaks at 628 nm, 621 nm, 707 nm, 713 nm, 730 nm, 738 nm. This peak that shows some signs of splitting and possibly some of these other features. Spectra was of this diamond was taken multiple times to exclude cosmic rays. Spectra of the surrounding substrate was also taken to rule out the peaks occurring from the substrate itself. It is unknown where a thallium contaminant might have come from.

Sample Ge had the most unknown spectrum peaks by far. Peaks were found at 636, 579, 704, 706, 667, 560, 613, 703, 628, 638, 643, 582, 705, 708 and 548 nm. Investigations into the origin of some of these peaks in ongoing.

The gym is the worst in January. It's not the worst because it's crowded. You love when the gym is crowded. Crowds equal witnesses. Witnesses equal attention. Attention is the primary source of muscle growth.

Dom Mazzetti

5 Conclusion

In this thesis, the development of a low temperature confocal microscope has been detailed. Every piece of this apparatus was either built or characterised during the development of this project and low temperature PL measurements are now routine in the QMAPP group. The utility of this confocal has been demonstrated by taking PL measurements of diamond samples at cryogenic temperatures, including characterisation of strain and thermal broadening.

The apparatus has many remarkable features, including high stability in many areas. The Red Pitaya driven mirrors show high mechanical stability. The cryostat shows high thermal stability. The extraordinarily low thermal drift brings incredible convenience for long measurements. The spectrometer that is high resolution over hundreds of nanometres changes the way spectral measurements are thought about.

There are several areas of extension of this work. Final optimisation of the set up needs to be carried out, and exciting new experiments are now possible. The collection efficiency needs to be thoroughly characterised and optimised. This could include a more optimal design, a different objective, or simply more efficient alignment. The ability to

detect single colour centre sites needs to be demonstrated as it is fundamental to many investigations. It wasn't important to do single site detection for characterising the samples of this thesis and the samples were not grown with this in mind. Thermal contact needs to be improved. Clamping the sample substrates onto the sample holder can not achieve the lowest temperatures otherwise possible. Getting diamond samples closer to direct contact with the cold finger is required.

It will soon be possible to perform high quality superradiance measurements at low temperatures. To look for evidence of superradiance, lifetime measurements need to be integrated in to the design. This is a relatively straight forward extension but has not been performed due to time constraints. Ideal samples for superradiance measurements still need to be found. The ability to select high quality samples by looking at strain environments makes this possible. While not directly related to this work, understanding why germanium is not being incorporated into the diamonds during CVD growth is an interesting topic. The lack of compelling evidence for GeV centres in the samples studied here is peculiar and not understood. This research will change how diamonds are grown within the QMAPP group when GeV centres are required.

University politics are vicious precisely because the stakes are so small.

Disputed origin

A

Python code to connect Red Pitaya to Qudi

A.1 Hardware module for Qudi

```
# -*- coding: utf-8 -*-

"""
This file contains the Qudi Hardware module Red Pitaya class.

Qudi is free software: you can redistribute it and/or modify
it under the terms of the GNU General Public License as published by
the Free Software Foundation, either version 3 of the License, or
(at your option) any later version.

Qudi is distributed in the hope that it will be useful,
but WITHOUT ANY WARRANTY; without even the implied warranty of
MERCHANTABILITY or FITNESS FOR A PARTICULAR PURPOSE.  See the
GNU General Public License for more details.

You should have received a copy of the GNU General Public License
along with Qudi. If not, see <http://www.gnu.org/licenses/>.

Copyright (c) the Qudi Developers. See the COPYRIGHT.txt file at the
```

```
20 top-level directory of this distribution and at <https://github.com/Ulm-IQO/qudi/>
21 """
22
23 import numpy as np
24 import time
25
26 from thirdparty.redpitaya import redpitaya_scpi as scpi
27
28 from core.module import Base, ConfigOption
29 from interface.gen_scanner_interface import GenScannerInterface
30 from interface.trigger_interface import TriggerInterface
31
32
33 class RedPitaya(Base, GenScannerInterface, TriggerInterface):
34     """ unstable: Matt Joliffe
35
36     A Red Pitaya device that can do lots of things.
37
38     An example config file entry 0would look like:
39
40     ```
41     # red_pitaya:
42     #     module.Class: 'red_pitaya.RedPitaya'
43     #     ip_address: '1.1.1.1'
44     #     scanner_ao_channels:
45     #         - 'OUT1'
46     #         - 'OUT2'
47     #     scanner_voltage_ranges:
48     #         - [-1, 1]
49     #         - [-1, 1]
50     #     trigger_out_channel: 'DIO1_P'
51     #     scanner_frequency:
52     #         - 10
53     #     scanner_position_ranges:
54     #         - [0, 1e-6]
55     #         - [0, 1e-6]
56     #     x_axis_inverted: 1
57     #     y_axis_inverted: 0
58     ```
59
60     """
61
62     _modtype = 'RPcard'
63     _modclass = 'hardware'
64
65     _ip = ConfigOption('ip_address', missing='error')
66     _scanner_ao_channels = ConfigOption('scanner_ao_channels', missing='error')
67     _scanner_voltage_ranges = ConfigOption('scanner_voltage_ranges', missing='error')
68     _scanner_frequency = ConfigOption('scanner_frequency', missing='error')
```

```
69      _trigger_out_channel = ConfigOption('trigger_out_channel', missing='warn')
70      _scanner_position_ranges = ConfigOption('scanner_position_ranges', missing='error')
71      _x_axis_inverted = ConfigOption('x_axis_inverted', missing='warn')
72      _y_axis_inverted = ConfigOption('y_axis_inverted', missing='warn')
73
74      def on_activate(self):
75          """ Starts up the RP Card at activation.
76          """
77          try:
78              self.rp_s = scpi.scpi(self._ip)
79          except:
80              self.log.error('Could not connect to Red Pitaya '+self._ip)
81
82          self.rp_s.tx_txt('ACQ:BUF:SIZE?')
83          self._buffer_size = int(self.rp_s.rx_txt())
84          self.rp_s.tx_txt('DIG:PIN:DIR OUT,'+ self._trigger_out_channel)
85
86          self.x_path_volt = [0,0]
87          self._scan_state = None
88          self._scanner_frequency = self._scanner_frequency[0]
89          self._pulse_duration = 1/self._scanner_frequency
90          self._trigger = 0
91          self._clock_frequency = self._scanner_frequency
92
93          # handle all the parameters given by the config
94
95          self._current_position = np.zeros(len(self._scanner_ao_channels))
96          self.set_position(x=self._scanner_position_ranges[0][0], y=self.
                _scanner_position_ranges[1][0])
97
98          if len(self._scanner_ao_channels) != len(self._scanner_voltage_ranges):
99              self.log.error(
100                 'Specify as many scanner_voltage_ranges as scanner_ao_channels!')
101         if len(self._scanner_ao_channels) != len(self._scanner_position_ranges):
102             self.log.error(
103                 'Specify as many scanner_position_ranges as scanner_ao_channels!')
104
105     def on_deactivate(self):
106         """ Shut down the Red Pitaya.
107         """
108         self.reset_hardware()
109
110     def scanner_on(self):
111         pass
112
113     ##########################################################################
114     # ================ GenerallScannerInterface Commands =====================
115     def reset_hardware(self):
116         """ Resets the Red Pitaya hardware.
```

```
117
118         @return int: error code (0:OK, -1:error)
119         """
120         try:
121             self.rp_s.tx_txt('GEN:RST')
122         except:
123             self.log.exception('Could not reset RedPitaya device at ' + self._ip)
124             return -1
125         return 0
126
127     def get_position_range(self):
128         """ Returns the physical range of the scanner.
129
130         @return float [2][2]: array of 2 ranges with an array containing lower
131                               and upper limit. The unit of the scan range is
132                               meters.
133         """
134         return self._scanner_position_ranges
135
136     def set_position_range(self, myrange=None):
137         """ Sets the physical position ranges. This can't actually be set by the software
                for RP.
138
139         @param float [2][2] myrange: array of 2 ranges with an array containing
140                                      lower and upper limit. The unit of the
141                                      scan range is meters.
142
143         @return int: error code (0:OK, -1:error)
144         """
145         self.log.info('This property cannot be configured with this device.')
146
147         return 0
148
149     def set_position(self, x=None, y=None, z=None, a=None):
150         """Move stage to x, y
151
152         @param float x: postion in x-direction (metres)
153         @param float y: postion in y-direction (metres)
154
155         @return int: error code (0:OK, -1:error)
156         """
157         if self.module_state() == 'locked': #TODO: check if this is necessary
158             self.log.error('Another scan_line is already running , close this one first.')
159             return -1
160
161         if z is not None or a is not None:
162             self.log.error('Can only set position in x and y axes')
163             return -1
164
```

```
165         if x is not None:
166             if not(self._scanner_position_ranges[0][0] <= x <= self.
                    _scanner_position_ranges[0][1]):
167                 self.log.error('You␣want␣to␣set␣x␣out␣of␣range:␣{0:f}.'.format(x))
168                 return -1
169             x_volt = self._scanner_position_to_volt(positions=[x], is_inverted=self.
                    _x_axis_inverted, axis=0)
170             x_volt = str(x_volt[0][0])
171             self._current_position[0] = np.float(x)
172 
173         if y is not None:
174             if not(self._scanner_position_ranges[1][0] <= y <= self.
                    _scanner_position_ranges[1][1]):
175                 self.log.error('You␣want␣to␣set␣y␣out␣of␣range:␣{0:f}.'.format(y))
176                 return -1
177             y_volt = self._scanner_position_to_volt(positions=[y], is_inverted=self.
                    _y_axis_inverted, axis=1)
178             y_volt = str(y_volt[0][0])
179             self._current_position[1] = np.float(y)
180 
181         try:
182             if x is not None and y is not None:
183                 self._red_pitaya_setpos(x=x_volt, y=y_volt)
184             elif x is not None:
185                 self._red_pitaya_setpos(x=x_volt)
186             else:
187                 self._red_pitaya_setpos(y=y_volt)
188             self._scan_state = '_set_pos'
189 
190             self.rp_s.tx_txt('TRIG:IMM')
191 
192             self.rp_s.tx_txt('OUTPUT1:STATE␣ON')
193         except:
194             self.log.warning('Cound␣not␣set␣position␣of␣RP␣device␣on␣'+ self._ip)
195             return -1
196         return 0
197 
198     def get_position(self):
199         """ Get the current position of the scanner hardware.
200 
201         @return float[]: current position in (x, y).
202         """
203         return self._current_position.tolist()
204 
205     def scan_line(self, line_path=None):
206         """ Scans a line.
207 
208         @param float[c][m] line_path: array of c-tuples defining the voltage points
209             (m = samples per line)
```

```
210
211         @return int: error code (0:OK, -1:error)
212
213         The input array looks for a xy scan of 5x5 points at the position y=1
214         like the following:
215             [ [1, 2, 3, 4, 5], [1, 1, 1, 1, 1]]
216         n is the number of scanner axes, which can vary. Typical values are 2 for galvo
                scanners,
217         """
218         if not isinstance(line_path, (frozenset, list, set, tuple, np.ndarray, ) ):
219             self.log.error('Given line_path list is not array type.')
220             return np.array([[-1.]])
221         self._trigger = 0
222
223         y_final = line_path[1][len(line_path[1])-1]
224         if line_path[1][0] != y_final:
225                 y_volt = self._scanner_position_to_volt(positions=[y_final], is_inverted=
                        self._y_axis_inverted, axis=1)
226                 y_volt = str(y_volt[0][0])
227
228                 self.rp_s.tx_txt('SOUR2:FUNC ARBITRARY')
229                 self.rp_s.tx_txt('SOUR2:TRAC:DATA:DATA ' + y_volt)
230                 self.rp_s.tx_txt('OUTPUT2:STATE ON')
231                 self._current_position[1] = np.float(y_final)
232                 return 0
233
234         if self.x_path_volt[0] != line_path[0][0] or self.x_path_volt[len(self.x_path_volt)
                -1] != line_path[0][len(line_path[0])-1] or self._scan_state !='_scanner':
235             self.set_up_line(line_path=line_path)
236
237         try:
238             self._scan_state = '_scanner'
239             self._trigger = 1
240             self._current_position[0] = np.array(line_path[0][0])
241         except:
242             self.log.exception('Error while scanning line.')
243             return -1
244         return 0
245
246     def scanner_off(self):
247         """ Closes the scanner.
248
249         @return int: error code (0:OK, -1:error)
250         """
251
252         try:
253             self.rp_s.tx_txt('GEN:RST')
254         except:
255             self.log.exception('Could not close analog on RP device on '+ self._ip)
```

```
256             return -1
257
258         return 0
259
260     def set_voltage_range(self, myrange=[-1,1],channel=[0,1]):
261         """ Set the voltage ranges for scanner.
262         @param float [2] myrange:
263         @param float [n] channel:
264         """
265         for axis in channel:
266             if axis > 1:
267                 self.log.error('Can only set axis 0 or 1 on this device')
268                 return -1
269         if myrange[0] < -1 or myrange[1] > 1:
270             self.log.error('Voltage must be between -1 and 1')
271             return -1
272         if myrange[0] >= myrange[1]:
273             self.log.error('Voltage range must go from low to high')
274             return -1
275         for axis in channel:
276             self._scanner_voltage_ranges[axis][0] = myrange[0]
277             self._scanner_voltage_ranges[axis][1] = myrange[1]
278         self._scan_state = None
279         return 0
280
281     def get_scanner_axes(self):
282         """ Return the axes of the scanner
283         @return float[] of the axes
284
285         """
286         return ['x','y']
287
288     def _set_scanner_speed(self, pixels=1):
289         """Set the scanning speed of the scanner in lines per second
290         @param float: Scanning speed in hertz
291         @return 0
292         """
293         frequency = self._clock_frequency/pixels
294         if frequency > 22:
295             self.log.warning('Speeds greater than 22 lines per second may cause timing
                issues')
296         self._scanner_frequency = frequency
297         self._pulse_duration = 1/frequency
298         return 0
299
300     def set_up_clock(self, clock_frequency=None):
301         self._clock_frequency = clock_frequency
302         self._scan_state = None
303
```

```
304
305     ##############################################################################
306     # ======== Private methods for GeneralScannerInterface Commands ===========
307
308     def set_up_line(self, line_path):
309         """ Sets up the analog output for scanning a line.
310
311         @param float[c][m] line_path: array of c-tuples defining the voltage points
312         (m = samples per line)
313
314         @return int: error code (0:OK, -1:error)
315         """
316
317         #if the scan path varies in y, set the y position to the final value, don't touch x
318         #dirty hack to prevent delays from writing positions to RP
319
320         #Red Pitaya does not like having a line path less than its buffer size
321         self.x_path_volt = np.linspace(line_path[0][0], line_path[0][len(line_path[0])-1],
                self._buffer_size)
322
323         x_path = self._scanner_position_to_volt(positions = self.x_path_volt, is_inverted=
                self._x_axis_inverted, axis=0)
324         try:
325             self.x_line = ''
326
327             for x_val in x_path:
328                 x_val = x_val[0]
329                 self.x_line += str(x_val) + ', '
330
331             self.x_line = self.x_line[:len(self.x_line)-2]
332
333             if self._scan_state != '_scanner':
334
335                 #set source 1,2 waveform to our scan values
336                 self._red_pitaya_scanline_setup(pixels=len(line_path[0]))
337                 self.rp_s.tx_txt('SOUR1:TRAC:DATA:DATA ' + self.x_line)
338                 self._red_pitaya_scanline_burstmode()
339                 self.rp_s.tx_txt('OUTPUT1:STATE ON')
340             else:
341                 self.rp_s.tx_txt('SOUR1:TRAC:DATA:DATA ' + self.x_line)
342             time.sleep(5) #debug
343         except:
344             self.log.exception('Could not set up scanline on RP device on '+ self._ip)
345             return -1
346
347         return 0
348
349     def _scanner_position_to_volt(self, is_inverted=0, positions=None, axis=0):
350         """ Converts a set of position pixels to acutal voltages.
```

```
351
352         @param float[n] positions: array of n-part tuples defining the pixels
353
354         @return float[n]: array of n-part tuples of corresponing voltages
355
356         """
357
358         #if not isinstance(positions, (frozenset, list, set, tuple, np.ndarray, )):
359         #    self.log.error('Given position list is no array type.')
360         #    return np.array([np.NaN])
361
362         vlist = []
363         for i in (positions):
364             vlist.append(
365                 (self._scanner_voltage_ranges[axis][1] - self._scanner_voltage_ranges[axis
                        ][0])
366                 / (self._scanner_position_ranges[axis][1] - self._scanner_position_ranges[
                        axis][0])
367                 * (i - self._scanner_position_ranges[axis][0])
368                 + self._scanner_voltage_ranges[axis][0]
369             )
370         if is_inverted == 1:
371             vlist = [-x for x in vlist]
372         volts = np.vstack(vlist)
373
374         if volts.min() < self._scanner_voltage_ranges[axis][0] or volts.max() > self.
                _scanner_voltage_ranges[axis][1]:
375             self.log.error(
376                 'Voltages ({0}, {1}) exceed the limit, the positions have to '
377                 'be adjusted to stay in the given range.'.format(volts.min(), volts.max()))
378             return np.array([np.NaN])
379         return volts
380
381     def _red_pitaya_scanline_setup(self, pixels=1):
382         """ Setup the Red Piatya to take an arbitrary scanline and set frequency.
383         @return 0
384         """
385         self.rp_s.tx_txt('SOUR1:FUNC ARBITRARY')
386         self._set_scanner_speed(pixels=pixels)
387         self.rp_s.tx_txt('SOUR1:FREQ:FIX ' + str(self._scanner_frequency))
388         return 0
389
390     def _red_pitaya_scanline_burstmode(self):
391         """ Set the Red Pitaya for burstmode scanning and external triggering
392         """
393         self.rp_s.tx_txt('SOUR1:BURS:NCYC 1')
394         self.rp_s.tx_txt('SOUR1:TRIG:SOUR EXT_PE')
395         self.rp_s.tx_txt('DIG:PIN:DIR OUT,'+ self._trigger_out_channel)
396         self.rp_s.tx_txt('DIG:PIN:DIR IN,DIO0_PE')
```

```
397
398         return 0
399
400     def _red_pitaya_setpos(self, x=None, y=None):
401         """Use Red Pitaya commands to set position.
402         @param float x: position in metres
403         @param float y: position in metres
404         """
405         self.rp_s.tx_txt('SOUR1:FUNC ARBITRARY')
406         self.rp_s.tx_txt('SOUR2:FUNC ARBITRARY')
407
408         self.rp_s.tx_txt('SOUR1:FREQ:FIX ' + str(self._scanner_frequency))
409         self.rp_s.tx_txt('SOUR2:FREQ:FIX ' + str(self._scanner_frequency))
410
411         #set source 1,2 waveform to our position values
412         try:
413             if x is not None:
414                 self.rp_s.tx_txt('SOUR1:TRAC:DATA:DATA ' + str(x))
415             if y is not None:
416                 self.rp_s.tx_txt('SOUR2:TRAC:DATA:DATA ' + str(y))
417
418             self.rp_s.tx_txt('OUTPUT1:STATE ON')
419             self.rp_s.tx_txt('OUTPUT2:STATE ON')
420             self.rp_s.tx_txt('TRIG:IMM')
421             return 0
422         except:
423             return -1
424
425
426     # ================ End ConfocalScannerInterface Commands ===================
427
428     # ================ TriggerInterface Commands ===============================
429
430     def set_pulse_amplitude(self, amplitude):
431         """Set the amplitude trigger pulse.
432         @param float: amplitude of pulse in volts
433         """
434         self.log.info('Can not set pulse amplitude on Red Pitaya. Amplitude is 3.3 V')
435         return 0
436
437     def set_pulse_duration(self, duration):
438         """Set the duration of the trigger pulse.
439         @param float: Set the duration of the pulse in seconds
440         """
441         self._pulse_duration = duration
442         return 0
443
444     def fire_trigger(self):
445         """Fire the trigger!
```

```
446         """
447         self.rp_s.tx_txt('DIG:PIN␣'+ self._trigger_out_channel+',␣1') #trigger on
448         time.sleep(self._pulse_duration)
449         self.rp_s.tx_txt('DIG:PIN␣'+ self._trigger_out_channel+',␣0') #trigger off
450         time.sleep(0.15) # Red pitaya has issues with rapidly self triggering
451 
452         return 0
453 
454     def gen_trigger(self, pin='DIO1_P'):
455         """Fire a general trigger!
456         @param str: The pin in which you want to trigger
457                     Pin will be of the form DIOM_P or DIOM_N
458                     where M is an int from 0-7
459         """
460         self.rp_s.tx_txt('DIG:PIN:DIR␣OUT,'+ pin)
461         self.rp_s.tx_txt('DIG:PIN␣'+ pin+',␣1')
462         time.sleep(self._pulse_duration)
463         self.rp_s.tx_txt('DIG:PIN␣'+ pin+',␣0')
464 
465         return 0
466     # ================ End TriggerInterface Commands ===================
```

A.2 Additional modules

An interfuse was created to join the Red Pitaya (operating the scanner, and also operating a hardware clock trigger signal) and the Swabian Instruments TimeTagger (counting the photons). Once fused with this module, this novel hardware combination plugged directly into the Qudi confocal microscope module. Full code for the interfuse module is browsable at https://github.com/QMAPP-mq/qudi/blob/6dfdd4d20d3834f1988336b370779469ea74f0eb/logic/interfuse/trigger_scanner_counter_interfuse.py

The Qudi confocal-scanner hardware interface is closely integrated with the National Instruments NI Card implementation. An interface was defined for a general scanner, and this code is browsable at https://github.com/QMAPP-mq/qudi/blob/4ee340578fbad805d7741117ffe39e6fac915e94/interface/gen_scanner_interface.py

References

[1] C. Bradac, M. T. Johnsson, M. v. Breugel, B. Q. Baragiola, R. Martin, M. L. Juan, G. K. Brennen, and T. Volz. *Room-temperature spontaneous superradiance from single diamond nanocrystals*. Nature Communications **8**(1), 1205 (2017). URL https://doi.org/10.1038/s41467-017-01397-4.

[2] R. H. Dicke. *Coherence in spontaneous radiation processes*. Phys. Rev. **93**, 99 (1954). URL https://link.aps.org/doi/10.1103/PhysRev.93.99.

[3] N. Skribanowitz, I. P. Herman, J. C. MacGillivray, and M. S. Feld. *Observation of dicke superradiance in optically pumped hf gas*. Phys. Rev. Lett. **30**, 309 (1973). URL https://link.aps.org/doi/10.1103/PhysRevLett.30.309.

[4] D. C. BURNHAM and R. Y. CHIAO. *Coherent resonance fluorescence excited by short light pulses*. Phys. Rev. **188**, 667 (1969). URL https://link.aps.org/doi/10.1103/PhysRev.188.667.

[5] M. Gross, C. Fabre, P. Pillet, and S. Haroche. *Observation of near-infrared dicke superradiance on cascading transitions in atomic sodium*. Phys. Rev. Lett. **36**, 1035 (1976). URL https://link.aps.org/doi/10.1103/PhysRevLett.36.1035.

[6] A. Flusberg, T. Mossberg, and S. Hartmann. *Observation of dicke superradiance at 1.30 micron in atomic ti vapor*. Physics Letters A **58**(6), 373 (1976). URL http://www.sciencedirect.com/science/article/pii/0375960176906678.

[7] H. M. Gibbs, Q. H. F. Vrehen, and H. M. J. Hikspoors. *Single-pulse superfluorescence in cesium*. Phys. Rev. Lett. **39**, 547 (1977). URL https://link.aps.org/doi/10.1103/PhysRevLett.39.547.

[8] R. Florian, L. Schwan, and D. Schmid. *Superradiance and high-gain mirrorless laser activity of o2-centers in kcl*. Solid State Communications **42**(1), 55 (1982). URL http://www.sciencedirect.com/science/article/pii/0038109882910286.

[9] A. Kumarakrishnan, S. Chudasama, and X. Han. *Collision-induced superfluorescence*. J. Opt. Soc. Am. B **22**(7), 1538 (2005). URL http://josab.osa.org/abstract.cfm?URI=josab-22-7-1538.

[10] F. P. BUNDY, H. T. HALL, H. M. STRONG, and R. H. WENTORF JUN. *Man-made diamonds*. Nature **176**, 51 EP (1955). URL http://dx.doi.org/10.1038/176051a0.

[11] A. M. Zaitsev. *Optical properties of diamond: a data handbook* (Springer Science & Business Media, 2001).

[12] M. W. Doherty, N. B. Manson, P. Delaney, F. Jelezko, J. Wrachtrup, and L. C. Hollenberg. *The nitrogen-vacancy colour centre in diamond*. Physics Reports **528**(1), 1 (2013).

[13] J. N. Becker and C. Becher. *Coherence properties and quantum control of silicon vacancy color centers in diamond*. physica status solidi (a) **214**(11), 1700586 (2017).

[14] T. Iwasaki, F. Ishibashi, Y. Miyamoto, Y. Doi, S. Kobayashi, T. Miyazaki, K. Tahara, K. D. Jahnke, L. J. Rogers, B. Naydenov, *et al. Germanium-vacancy single color centers in diamond*. Scientific reports **5**, 12882 (2015).

[15] G. Davies. and M. F. Hamer. *Optical studies of the 1.945 ev vibronic band in diamond*. Proceedings of the Royal Society of London A: Mathematical, Physical and Engineering Sciences **348**(1653), 285 (1976). http://rspa.royalsocietypublishing.org/content/348/1653/285.full.pdf, URL http://rspa.royalsocietypublishing.org/content/348/1653/285.

[16] G. Balasubramanian, P. Neumann, D. Twitchen, M. Markham, R. Kolesov, N. Mizuochi, J. Isoya, J. Achard, J. Beck, J. Tissler, *et al. Ultralong spin coherence time in isotopically engineered diamond*. Nature materials **8**(5), 383 (2009).

[17] C. Santori, P. Tamarat, P. Neumann, J. Wrachtrup, D. Fattal, R. G. Beausoleil, J. Rabeau, P. Olivero, A. D. Greentree, S. Prawer, *et al. Coherent population trapping of single spins in diamond under optical excitation*. Physical Review Letters **97**(24), 247401 (2006).

[18] J. Jeske, D. W. M. Lau, X. Vidal, L. P. McGuinness, P. Reineck, B. C. Johnson, M. W. Doherty, J. C. McCallum, S. Onoda, F. Jelezko, T. Ohshima, T. Volz, J. H. Cole, B. C. Gibson, and A. D. Greentree. *Stimulated emission from nitrogen-vacancy centres in diamond*. Nature Communications **8**, 14000 EP (2017). Article, URL http://dx.doi.org/10.1038/ncomms14000.

[19] V. S. Vavilov, A. A. Gippius, A. M. Zaitsev, B. V. Derjaguin, B. V. Spitsyn, and A. E. Aleksenko. *??* Sov. Phys.-Semicond. **14**, 1078 (1980).

[20] C. D. Clark, H. Kanda, I. Kiflawi, and G. Sittas. *Silicon defects in diamond*. Phys. Rev. B **51**, 16681 (1995). URL https://link.aps.org/doi/10.1103/PhysRevB.51.16681.

[21] J. P. Goss, R. Jones, S. J. Breuer, P. R. Briddon, and S. Öberg. *The twelve-line 1.682 ev luminescence center in diamond and the vacancy-silicon complex*. Phys. Rev. Lett. **77**, 3041 (1996). URL https://link.aps.org/doi/10.1103/PhysRevLett.77.3041.

[22] U. D'Haenens-Johansson, A. Edmonds, B. Green, M. Newton, G. Davies, P. Martineau, R. Khan, and D. Twitchen. *Optical properties of the neutral silicon split-vacancy center in diamond*. Physical Review B **84**(24), 245208 (2011).

[23] C. Hepp, T. Müller, V. Waselowski, J. N. Becker, B. Pingault, H. Sternschulte, D. Steinmüller-Nethl, A. Gali, J. R. Maze, M. Atatüre, and C. Becher. *Electronic structure of the silicon vacancy color center in diamond*. Phys. Rev. Lett. **112**, 036405 (2014). URL https://link.aps.org/doi/10.1103/PhysRevLett.112.036405.

[24] L. J. Rogers, K. D. Jahnke, M. W. Doherty, A. Dietrich, L. P. McGuinness, C. Müller, T. Teraji, H. Sumiya, J. Isoya, N. B. Manson, *et al. Electronic structure of the negatively charged silicon-vacancy center in diamond*. Physical Review B **89**(23), 235101 (2014).

[25] C. Wang, C. Kurtsiefer, H. Weinfurter, and B. Burchard. *Single photon emission from siv centres in diamond produced by ion implantation*. Journal of Physics B: Atomic, Molecular and Optical Physics **39**(1), 37 (2006). URL http://stacks.iop.org/0953-4075/39/i=1/a=005.

[26] E. Neu, D. Steinmetz, J. Riedrich-MÃČÂűller, S. Gsell, M. Fischer, M. Schreck, and C. Becher. *Single photon emission from silicon-vacancy colour centres in chemical*

vapour deposition nano-diamonds on iridium. New Journal of Physics **13**(2), 025012 (2011). URL http://stacks.iop.org/1367-2630/13/i=2/a=025012.

[27] J. C. Lee, I. Aharonovich, A. P. Magyar, F. Rol, and E. L. Hu. *Coupling of silicon-vacancy centers to a single crystal diamond cavity*. Optics express **20**(8), 8891 (2012).

[28] L. J. Rogers, K. D. Jahnke, T. Teraji, L. Marseglia, C. Müller, B. Naydenov, H. Schauffert, C. Kranz, J. Isoya, L. P. McGuinness, and F. Jelezko. *Multiple intrinsically identical single-photon emitters in the solid state*. Nature Communications **5**, 4739 EP (2014). Article, URL http://dx.doi.org/10.1038/ncomms5739.

[29] J. Riedrich-Moller, C. Arend, C. Pauly, F. MuÌĹcklich, M. Fischer, S. Gsell, M. Schreck, and C. Becher. *Deterministic coupling of a single silicon-vacancy color center to a photonic crystal cavity in diamond*. Nano letters **14**(9), 5281 (2014).

[30] M. Leifgen, T. Schröder, F. Gädeke, R. Riemann, V. Métillon, E. Neu, C. Hepp, C. Arend, C. Becher, K. Lauritsen, *et al. Evaluation of nitrogen-and silicon-vacancy defect centres as single photon sources in quantum key distribution*. New journal of physics **16**(2), 023021 (2014).

[31] A. Sipahigil, K. D. Jahnke, L. J. Rogers, T. Teraji, J. Isoya, A. S. Zibrov, F. Jelezko, and M. D. Lukin. *Indistinguishable photons from separated silicon-vacancy centers in diamond*. Phys. Rev. Lett. **113**, 113602 (2014). URL https://link.aps.org/doi/10.1103/PhysRevLett.113.113602.

[32] T. Müller, C. Hepp, B. Pingault, E. Neu, S. Gsell, M. Schreck, H. Sternschulte, D. Steinmüller-Nethl, C. Becher, and M. Atatüre. *Optical signatures of silicon-vacancy spins in diamond*. Nature Communications **5**, 3328 EP (2014). Article, URL http://dx.doi.org/10.1038/ncomms4328.

[33] L. J. Rogers, K. D. Jahnke, M. H. Metsch, A. Sipahigil, J. M. Binder, T. Teraji, H. Sumiya, J. Isoya, M. D. Lukin, P. Hemmer, *et al. All-optical initialization, readout, and coherent preparation of single silicon-vacancy spins in diamond*. Physical review letters **113**(26), 263602 (2014).

[34] B. Pingault, J. N. Becker, C. H. Schulte, C. Arend, C. Hepp, T. Godde, A. I. Tartakovskii,

M. Markham, C. Becher, and M. Atatüre. *All-optical formation of coherent dark states of silicon-vacancy spins in diamond*. Physical review letters **113**(26), 263601 (2014).

[35] K. D. Jahnke, A. Sipahigil, J. M. Binder, M. W. Doherty, M. Metsch, L. J. Rogers, N. B. Manson, M. D. Lukin, and F. Jelezko. *Electron–phonon processes of the silicon-vacancy centre in diamond*. New Journal of Physics **17**(4), 043011 (2015).

[36] T. Schröder, M. E. Trusheim, M. Walsh, L. Li, J. Zheng, M. Schukraft, A. Sipahigil, R. E. Evans, D. D. Sukachev, C. T. Nguyen, J. L. Pacheco, R. M. Camacho, E. S. Bielejec, M. D. Lukin, and D. Englund. *Scalable focused ion beam creation of nearly lifetime-limited single quantum emitters in diamond nanostructures*. Nature Communications **8**, 15376 EP (2017). Article, URL http://dx.doi.org/10.1038/ncomms15376.

[37] U. Jantzen, A. B. Kurz, D. S. Rudnicki, C. SchÃČÂďermeier, K. D. Jahnke, U. L. Andersen, V. A. Davydov, V. N. Agafonov, A. Kubanek, L. J. Rogers, and F. Jelezko. *Nanodiamonds carrying silicon-vacancy quantum emitters with almost lifetime-limited linewidths*. New Journal of Physics **18**(7), 073036 (2016). URL http://stacks.iop.org/1367-2630/18/i=7/a=073036.

[38] L. J. Rogers, O. Wang, Y. Liu, L. Antoniuk, C. Osterkamp, V. A. Davydov, V. N. Agafonov, A. B. Filipovski, F. Jelezko, and A. Kubanek. *Single SiV^- centers in low-strain nanodiamonds with bulk-like spectral properties and nano-manipulation capabilities*. ArXiv e-prints (2018). 1802.03588.

[39] P. Siyushev, M. H. Metsch, A. Ijaz, J. M. Binder, M. K. Bhaskar, D. D. Sukachev, A. Sipahigil, R. E. Evans, C. T. Nguyen, M. D. Lukin, *et al.* *Optical and microwave control of germanium-vacancy center spins in diamond*. Physical Review B **96**(8), 081201 (2017).

[40] E. A. Ekimov, S. Lyapin, K. N. Boldyrev, M. V. Kondrin, R. Khmelnitskiy, V. A. Gavva, T. V. Kotereva, and M. N. Popova. *Germanium–vacancy color center in isotopically enriched diamonds synthesized at high pressures*. JETP letters **102**(11), 701 (2015).

[41] M. K. Bhaskar, D. D. Sukachev, A. Sipahigil, R. E. Evans, M. J. Burek, C. T. Nguyen, L. J. Rogers, P. Siyushev, M. H. Metsch, H. Park, *et al.* *Quantum nonlinear optics with a germanium-vacancy color center in a nanoscale diamond waveguide*. Physical review letters **118**(22), 223603 (2017).

[42] L. Rogers. *How far into the infrared can a colour centre in diamond emit?* Physics Procedia **3**(4), 1557 (2010).

[43] A. Gruber, A. Dräbenstedt, C. Tietz, L. Fleury, J. Wrachtrup, and C. v. Borczyskowski. *Scanning confocal optical microscopy and magnetic resonance on single defect centers*. Science **276**(5321), 2012 (1997). http://science.sciencemag.org/content/276/5321/2012.full.pdf, URL http://science.sciencemag.org/content/276/5321/2012.

[44] J. M. Binder, A. Stark, N. Tomek, J. Scheuer, F. Frank, K. D. Jahnke, C. MÃijller, S. Schmitt, M. H. Metsch, T. Unden, T. Gehring, A. Huck, U. L. Andersen, L. J. Rogers, and F. Jelezko. *Qudi: A modular python suite for experiment control and data processing*. SoftwareX **6**, 85 (2017). URL http://www.sciencedirect.com/science/article/pii/S2352711017300055.

[45] T. Feger, C. Schwab, B. C. K. Tiong, M. J. Ireland, A. Rains, and D. W. Coutts. *The rhea single-mode spectrograph*. In *Ground-based and Airborne Instrumentation for Astronomy VII*, vol. 10702, p. 1070253 (International Society for Optics and Photonics, 2018).